Galerkin boundary integral equation method for spontaneous rupture propagation problems: SH-case

Hiroyuki Goto[1] and Jacobo Bielak[2]

[1] *Disaster Prevention Research Institute, Kyoto University, Gokasho, Uji, Kyoto, Japan.*
E-mail: goto@catfish.dpri.kyoto-u.ac.jp
[2] *Computational Seismology Laboratory, Department of Civil and Environmental Engineering, Carnegie Mellon University, Pittsburgh, PA, USA.*
E-mail: jbielak@cmu.edu

Accepted 2007 November 22. Received 2007 November 1; in original form 2007 May 13

SUMMARY

We develop a Galerkin finite element boundary integral equation method (GaBIEM) for spontaneous rupture propagation problems for a planar fault embedded in a homogeneous full 2D space. A 2D antiplane rupture propagation problem, with a slip-weakening friction law, is simulated by the GaBIEM. This method allows one to eliminate the strong singularities from the integral representation of the traction, and to separate explicitly the expression for the traction into an instantaneous component; static and time-dependent components with weakly (logarithmic) singular kernels; and a dynamic component and a quasi-static component, with continuous, bounded, kernels. Simulated results throw light into the performance of the GaBIEM and highlight differences with respect to that of the traditional, collocation, boundary integral equation method (BIEM). Both methods converge with a power law with respect to grid size, with different exponents. There is no restriction on the CFL stability number for the GaBIEM since an implicit, unconditionally stable method is used for the time integration. The error of the approximation increases with the time step, as expected, and it can remain below that of the BIEM.

Key words: rupture propagation, elastodynamics

1 INTRODUCTION

Dynamic rupture simulations have revealed physical aspects of earthquake rupture propagations along the fault that differ significantly from that of kinematic sources. This has been demonstrated through a number of realistic models for several historical earthquakes, e.g. 1989 Loma Prieta earthquake [Bouchon, 1997], 1992 Landers earthquake [Aochi and Fukuyama, 2002] and 2000 Tottori earthquake [Dalguer *et al.*, 2003]. Several computational schemes have been developed in order to simulate the complex rupture behavior, e.g. the boundary integral equation method [Das and Aki, 1977a,b, Das, 1980, Das, 1981, Andrews, 1985], finite differences [Andrews, 1976a, Day, 1982, Madariaga *et al.*, 1998, Andrews, 1999, Dalguer and Day, 2007] and finite elements [Oglesby and Archuleta, 2000a, Oglesby *et al.*, 2000b, Aagaard *et al.*, 2001, Oglesby and Archuleta, 2003]. The time-domain traction boundary integral equation method (BIEM), proposed by Koller *et al.* (1992) for 2D-problems, provides an accurate and efficient computational scheme for simple models, e.g. a planar fault in a homogeneous full space medium; such methods have been extended, e.g. by Cochard and Madariaga (1994) to 2D- and by Fukuyama and Madariaga (1998) for 3D-problems. Other authors have subsequently relaxed some of the simplifying assumptions, e.g. the BIEM to non-planar fault in 2D [Tada and Yamashita, 1997], 3D full space [Tada *et al.*, 2000] and 3D half space [Zhang and Chen, 2006a,b]. Some authors suggested to separate the radiation damping terms from the elastodynamic convolutions for earthquake cycle simulations into static and dynamic components in order to reduce the expensive calculations [Ben-Zion and Rice, 1997, Lapusta *et al.*, 2000, Lapusta and Rice, 2003].

The Galerkin method, based on weighted residual techniques, provides a means for eliminating the hyper-singularities that occur in the boundary integral equation formulation and also supports energy consistent solutions. The Galerkin boundary integral equation method (GaBIEM) has been used for various engineering applications [e.g. Zeng and Bielak, 1994, Chien and Atkinson, 1997, Li and Mear, 1998, Yoshida and Nishimura, 2001, Kallivokas *et al.*, 2005]. In particular, Yoshida and Nishimura (2001) used fast multipole GaBIEM for static crack opening problems and Kallivokas *et al.* (2005) used a symmetric GaBIEM for multi-domain interface problems.

In this paper, we present the derivation of GaBIEM for spontaneous rupture propagation problems in the context of simple 2D antiplane

rupture propagation, and compare it with the traditional BIEM. We also examine the physical meaning of the various terms in the GaBIEM and assess its numerical performance.

2 BOUNDARY INTEGRAL EQUATION

2.1 Formulation

Let S be a single planar fault embedded in a homogeneous elastic full 2D space V. x_1 and x_2 are Cartesian coordinates, and x_1 is directed along the fault S as shown in Fig. 1. This paper focuses on the antiplane case consisting of shear slip displacement $\Delta u(x_1, t)$ in the rupture propagation direction of x_1, where t is time. The antiplane slip displacement is perpendicular to the plane formed by x_1 and x_2, and is defined as,

$$\Delta u(x_1, t) = \lim_{\varepsilon \to +0} [u(x_1 + \varepsilon, t) - u(x_1 - \varepsilon, t)], \tag{1}$$

where u is the only nonvanishing displacement, in the x_3 direction. The first space derivative of the slip displacement, $\partial \Delta u / \partial x_1$, has a discontinuity at the rupture front. Since the second derivative of the slip displacement then entails a Dirac delta function, one then tries to avoid this derivative in the formulation of the governing boundary integral equation. This problem was originally treated by Cochard and Madariaga (1994) in 2D and subsequently by Tada and Yamashita (1997), Fukuyama and Madariaga (1998), and Tada *et al.* (2000) in 3D. Cochard and Madariaga (1994) were the first researches in seismology to use integration by parts to regularize the hypersingularity in the integral representation; through integration by parts and various additional manipulations they obtained the relationship between the instantaneous change in slip velocity and the traction change. Our approach, partly inspired by Cochard and Madariaga (1994), is different in some important respects from earlier formulations and leads for the antiplane case considered here to at most weakly singular (logarithmic) kernels, as opposed to that of Cochard and Madariaga (1994), which includes a Cauchy-type singularity.

The displacement u is generally represented by the following boundary integral [Aki and Richards, 2000]:

$$u(x_1, x_2, t) = - \int_0^t d\tau \int_S \Delta u(\xi, \tau) \cdot \mu \cdot \frac{\partial}{\partial x_2} G(x_1, x_2, t; \xi, \tau) \cdot d\xi, \tag{2}$$

where μ is the rigidity of the material. The normal direction of S is parallel to the direction of x_2. G is the Green's function corresponding to the 2D SH wave field in a homogeneous full space,

$$G(x_1, x_2, t; \xi, \tau) = \frac{1}{2\pi\mu} \cdot \frac{1}{\sqrt{(t-\tau)^2 - r^2/\beta^2}} \cdot H(t - \tau - r/\beta), \tag{3}$$

in which $r = \sqrt{(x_1 - \xi)^2 + x_2^2}$, β is S-wave velocity, ξ is the point on the fault where a unit load is applied, τ the instant at which it is applied, and $H(t)$ is the Heaviside step function.

Stresses σ everywhere in V can be derived from Eq.(2) and from these one obtains the traction T on the fault as the limiting value of the stress on the fault. Since the fault is aligned with the x_1 axis, only the x_2-component of the stress, σ_2, needs to be considered. Let (x_1,x_2) be a point in V. Then,

$$\sigma_2(x_1, x_2, t) = \mu \cdot \frac{\partial}{\partial x_2} u(x_1, x_2, t) = -\mu \int_0^t d\tau \int_S \Delta u(\xi, \tau) \cdot \mu \cdot \frac{\partial^2}{\partial {x_2}^2} G(x_1, x_2, t; \xi, \tau) \cdot d\xi. \tag{4}$$

Since by definition, G is a fundamental solution of the wave equation [Fukuyama and Madariaga, 1998, Tada *et al.*, 2000], away from the fault, G satisfies the equation.

$$\frac{1}{\beta^2} \ddot{G} = \frac{\partial^2}{\partial {x_1}^2} G + \frac{\partial^2}{\partial {x_2}^2} G. \tag{5}$$

With this equation, the second derivative of G with respect to x_2 can be replaced by the terms of the second derivatives with respect to t and x_1, as follows,

$$\begin{aligned} \sigma_2(x_1, x_2, t) = & - \frac{\mu^2}{\beta^2} \int_0^t d\tau \int_S \Delta u(\xi, \tau) \cdot \ddot{G}(x_1, x_2, t; \xi, \tau) \cdot d\xi \\ & + \mu^2 \int_0^t d\tau \int_S \Delta u(\xi, \tau) \cdot \frac{\partial^2}{\partial {x_1}^2} G(x_1, x_2, t; \xi, \tau) \cdot d\xi \qquad (6) \\ = & - \frac{\mu^2}{\beta^2} \int_0^t d\tau \int_S \Delta \ddot{u}(\xi, \tau) \cdot G(x_1, x_2, t; \xi, \tau) \cdot d\xi \\ & - \mu^2 \int_0^t d\tau \int_S \Delta u(\xi, \tau) \cdot \frac{\partial^2}{\partial \xi \partial x_1} G(x_1, x_2, t; \xi, \tau) \cdot d\xi, \qquad (7) \end{aligned}$$

where the derivation includes integration by parts in time with G satisfying zero initial conditions, and the identity $\partial G / \partial \xi = -\partial G / \partial x_1$.

Following Cochard and Madariaga (1994), the second term is treated by using integration by parts in space:

$$\sigma_2(x_1,x_2,t) = -\frac{\mu^2}{\beta^2}\int_0^t d\tau \int_S \Delta\ddot{u}(\xi,\tau)\cdot G(x_1,x_2,t;\xi,\tau)\cdot d\xi + \mu^2\int_0^t d\tau\int_S \frac{\partial}{\partial\xi}\Delta u(\xi,\tau)\cdot\frac{\partial}{\partial x_1}G(x_1,x_2,t;\xi,\tau)\cdot d\xi. \tag{8}$$

Then, the limit of the stress on the fault plane gives the traction $T(x_1,t)$.

$$T(x_1,t) = \lim_{x_2\to+0}\sigma_2(x_1,x_2,t) = -\frac{\mu^2}{\beta^2}\int_0^t d\tau \int_S \Delta\ddot{u}(\xi,\tau)\cdot G(x_1,t;\xi,\tau)\cdot d\xi + \mu^2\int_0^t d\tau\int_S \frac{\partial}{\partial\xi}\Delta u(\xi,\tau)\cdot\frac{\partial}{\partial x_1}G(x_1,t;\xi,\tau)\cdot d\xi. \tag{9}$$

Equation (9) is a boundary integral equation (BIE) for the slip in the antiplane planar fault in a homogeneous full 2D space. However, this formulation still contains strong singularities, and is not readily amenable to numerical approximations.

2.2 Regularization of the boundary integral equation

Let Eq.(9) be written as:

$$\begin{aligned} T(x_1,t) = &-\frac{\mu^2}{\beta^2}\int_0^t d\tau\int_{-\infty}^{\infty}\Delta\ddot{u}(x_1,\tau)\cdot G(x_1,t;\xi,\tau)\cdot d\xi \\ &-\frac{\mu^2}{\beta^2}\int_0^t d\tau\int_{-\infty}^{\infty}[\Delta\ddot{u}(\xi,\tau)-\Delta\ddot{u}(x_1,\tau)]\cdot G(x_1,t;\xi,\tau)\cdot d\xi \\ &+\mu^2\int_0^t d\tau\int_S\frac{\partial}{\partial\xi}\Delta u(\xi,\tau)\cdot\frac{\partial}{\partial x_1}G(x_1,t;\xi,\tau)\cdot d\xi, \end{aligned} \tag{10}$$

in which we have added and subtracted the term containing $\Delta\ddot{u}(x_1,t)$. Note that the first and second terms in this equation are integrated over an infinite range instead of S. This substitution is valid because slip does not occur in the complement region of S.

The first term of Eq.(10) involves the spatial integration of the Green's function over the infinite domain. This integral evaluated analytically:

$$\begin{aligned} \int_{-\infty}^{\infty}G(x_1,t;\xi,\tau)\cdot d\xi &= \int_{x_1-\beta(t-\tau)}^{x_1+\beta(t-\tau)}\frac{1}{2\pi\mu}\cdot\frac{1}{\sqrt{(t-\tau)^2-(x_1-\xi)^2/\beta^2}}\cdot d\xi \\ &= \int_{-(t-\tau)}^{t-\tau}\frac{\beta}{2\pi\mu}\cdot\frac{dp}{\sqrt{(t-\tau)^2-p^2}} = \frac{\beta}{2\mu} \end{aligned} \tag{11}$$

Eq.(11) obviously provides a result that is independent of τ. Therefore, the slip acceleration in the first term of Eq.(10) is directly integrable in τ:

$$-\frac{\mu^2}{\beta^2}\int_0^t d\tau\int_{-\infty}^{\infty}\Delta\ddot{u}(x_1,\tau)\cdot G(x_1,t;\xi,\tau)\cdot d\xi = -\frac{\mu}{2\beta}\Delta\dot{u}(x_1,t). \tag{12}$$

This is the same term that appears in the derivation of Cochard and Madariaga (1994) in agreement with Brune (1970), who obtained it using physical arguments. The second term of Eq.(10) contains infinite integration in space, which is difficult to evaluate numerically. Thus, we first integrate by parts to eliminate $\Delta\ddot{u}(x_1,\tau)$ and avoid the infinite integration. That is,

$$\begin{aligned} &-\frac{\mu^2}{\beta^2}\int_0^t d\tau\int_{-\infty}^{\infty}[\Delta\ddot{u}(\xi,\tau)-\Delta\ddot{u}(x_1,\tau)]\cdot G(x_1,t;\xi,\tau)\cdot d\xi \\ =&\frac{\mu^2}{\beta^2}\int_0^t d\tau\int_S\frac{\partial}{\partial\xi}\Delta\ddot{u}(\xi,\tau)\cdot\tilde{G}(x_1,t;\xi,\tau)\cdot d\xi = \int_0^t d\tau\int_S\rho\frac{\partial}{\partial\xi}\Delta\ddot{u}(\xi,\tau)\cdot\mu\tilde{G}(x_1,t;\xi,\tau)\cdot d\xi, \end{aligned} \tag{13}$$

where

$$\tilde{G}(x_1,t;\xi,\tau) = \frac{\beta}{2\pi\mu}\left[\frac{\pi}{2}\operatorname{sgn}(x_1-\xi)-\sin^{-1}\left(\frac{x_1-\xi}{\beta(t-\tau)}\right)\right]\cdot H\left(t-\tau-|x_1-\xi|/\beta\right). \tag{14}$$

To avoid the singularity that appears in the third term in Eq.(10), we integrate by parts in time:

$$\mu^2\int_0^t d\tau\int_S\frac{\partial}{\partial\xi}\Delta u(\xi,\tau)\cdot\frac{\partial}{\partial x_1}G(x_1,t;\xi,\tau)\cdot d\xi = \mu^2\int_0^t d\tau\int_S\frac{\partial}{\partial\xi}\Delta\dot{u}(\xi,\tau)\cdot\frac{\partial}{\partial x_1}\bar{G}(x_1,t;\xi,\tau)\cdot d\xi, \tag{15}$$

where

$$\bar{G}(x_1,t;\xi,\tau) = \frac{1}{2\pi\mu}\log\left[\frac{\beta(t-\tau)}{|x_1-\xi|}-\sqrt{\frac{\beta^2(t-\tau)^2}{(x_1-\xi)^2}-1}\right]\cdot H\left(t-\tau-|x_1-\xi|/\beta\right). \tag{16}$$

With these operations, Eq.(10) becomes:

$$T(x_1,t) = -\frac{\mu}{2\beta}\Delta\dot{u}(x_1,t) + \int_0^t d\tau \int_S \rho\frac{\partial}{\partial\xi}\Delta\ddot{u}(\xi,\tau)\cdot\mu\tilde{G}(x_1,t;\xi,\tau)\cdot d\xi + \mu^2\int_0^t d\tau\int_S \frac{\partial}{\partial\xi}\Delta\dot{u}(\xi,\tau)\cdot\frac{\partial}{\partial x_1}\bar{G}(x_1,t;\xi,\tau)\cdot d\xi, \tag{17}$$

where $\tilde{G}$ and $\bar{G}$ are defined in Eqs.(14) and (16), respectively. The first term in Eq.(17) represents the instantaneous response from the slip distribution over the whole fault plane. It is directly proportional to the slip at every instant and at each point on the plane of the fault. Therefore, we call it the "Instantaneous term". The second term, which is the only one in which the mass density appears separately from the shear modulus or shear velocity, represents an inertial force contributed by the slip acceleration. We call the second term "Dynamic term". The third term is similar to the static traction T^S which is represented as,

$$T^S(x_1) = \mu^2\int_S \frac{\partial}{\partial\xi}\Delta u(\xi)\cdot\frac{\partial}{\partial x_1}G^S(x_1;\xi)\cdot d\xi, \tag{18}$$

where G^S is static Green's function.

$$G^S(x_1;\xi) = \frac{1}{2\pi\mu}\log\left[\frac{1}{|x_1-\xi|}\right]. \tag{19}$$

As we will describe later, the residual traction distribution governed by this third term in Eq.(17) reduces to the static traction for the long-term solution. We then call the third term the "Quasi-static" component of traction.

3 GALERKIN BOUNDARY INTEGRAL EQUATION METHOD

Galerkin's method is most often used to solve numerically boundary-value or initial-value problems defined by partial differential equations, usually in the form of the finite element method. For the boundary integral equation, several applications of the Galerkin's method have been reported in engineerings [e.g. Zeng and Bielak, 1994, Chien and Atkinson, 1997, Li and Mear, 1998, Yoshida *et al.*, 2001, Kallivokas *et al.*, 2005]. Here, we apply Galerkin's method to the boundary integral equation for spontaneous rupture propagation.

3.1 Weak form of the boundary integral equation

When S is selected as the whole rupture propagation area, $\Delta u(x_1,t)$ satisfies homogeneous conditions at the boundary of S. We obtain the weak form of our problem by multiplying Eq.(17) by an arbitrary piecewise continuous test function $v(x_1)$, which satisfies the same boundary condition as $\Delta u(x_1)$, and integrating over S:

$$\begin{aligned}\int_S T(x_1,t)\cdot v(x_1)\cdot dx_1 = &\int_S -\frac{\mu}{2\beta}\Delta\dot{u}(x_1,t)\cdot v(x_1)\cdot dx_1 \\ &+\int_S\int_S\int_0^t \rho\frac{\partial}{\partial\xi}\Delta\ddot{u}(\xi,\tau)\cdot\mu\tilde{G}(x_1,t;\xi,\tau)\cdot d\tau d\xi\cdot v(x_1)\cdot dx_1 \\ &+\int_S\int_S\int_0^t \mu^2\frac{\partial}{\partial\xi}\Delta\dot{u}(\xi,\tau)\cdot\frac{\partial}{\partial x_1}\bar{G}(x_1,t;\xi,\tau)\cdot d\tau d\xi\cdot v(x_1)\cdot dx_1.\end{aligned} \tag{20}$$

Now, to reduce the order of the singularity associated with the spatial derivative of $\bar{G}$, we integrate the third term in Eq.(20) by parts. There will be no contribution from the boundary of S because of the condition that v vanish on that boundary. There results:

$$\begin{aligned}\int_S T(x_1,t)\cdot v(x_1)\cdot dx_1 = &\int_S -\frac{\mu}{2\beta}\Delta\dot{u}(x_1,t)\cdot v(x_1)\cdot dx_1 \\ &+\int_S\int_S\int_0^t \rho\frac{\partial}{\partial\xi}\Delta\ddot{u}(\xi,\tau)\cdot\mu\tilde{G}(x_1,t;\xi,\tau)\cdot v(x_1)\cdot d\tau d\xi dx_1 \\ &-\int_S\int_S\int_0^t \mu^2\frac{\partial}{\partial\xi}\Delta\dot{u}(\xi,\tau)\cdot\bar{G}(x_1,t;\xi,\tau)\cdot\frac{\partial}{\partial x_1}v(x_1)\cdot d\tau d\xi dx_1.\end{aligned} \tag{21}$$

This equation gives the weak form for the traction T in terms of the slip-rate $\Delta\dot{u}$ and its first derivative. The third term in this equation can be written in a physically more meaningful form if we make explicit use of the expression for the kernel $\bar{G}$. Multiplying the numerator and denominator of the argument of the logarithm in Eq.(16) by its conjugate, the last term in Eq.(21) can be rewritten as:

$$\begin{aligned}&\int_S\int_S\int_0^t \mu^2\frac{\partial}{\partial\xi}\Delta\dot{u}(\xi,\tau)\cdot\bar{G}(x_1,t;\xi,\tau)\cdot\frac{\partial}{\partial x_1}v(x_1)\cdot d\tau d\xi dx_1 \\ =&\frac{\mu}{2\pi}\int_S\int_S\int_0^t\left\{\left[\frac{\partial}{\partial\xi}\Delta\dot{u}(\xi,\tau)\cdot\log\frac{|x_1-\xi|}{\beta(t-\tau)}\cdot\frac{\partial}{\partial x_1}v(x_1)\right.\right. \\ -&\left.\left.-\frac{\partial}{\partial\xi}\Delta\dot{u}(\xi,\tau)\check{G}(x_1,t;\xi,\tau)\cdot\frac{\partial}{\partial x_1}v(x_1)\right]\cdot H(t-\tau-|x_1-\xi|/\beta)\right\}\cdot d\tau d\xi dx_1\end{aligned} \tag{22}$$

or, for convenience, splitting the logarithmic kernel,

$$\begin{aligned}
&\int_S\int_S\int_0^t \mu^2\frac{\partial}{\partial\xi}\Delta\dot{u}(\xi,\tau)\cdot\bar{G}(x_1,t;\xi,\tau)\cdot\frac{\partial}{\partial x_1}v(x_1)\cdot d\tau d\xi dx_1\\
=&\frac{\mu}{2\pi}\int_S\int_S\int_0^t\left\{\left[\frac{\partial}{\partial\xi}\Delta\dot{u}(\xi,\tau)\cdot\log\frac{|x_1-\xi|}{L}\cdot\frac{\partial}{\partial x_1}v(x_1)-\frac{\partial}{\partial\xi}\Delta\dot{u}(\xi,\tau)\cdot\log\frac{\beta(t-\tau)}{L}\cdot\frac{\partial}{\partial x_1}v(x_1)\right.\right.\\
-&\left.\left.\frac{\partial}{\partial\xi}\Delta\dot{u}(\xi,\tau)\cdot\check{G}(x_1,t;\xi,\tau)\cdot\frac{\partial}{\partial x_1}v(x_1)\right]\cdot H(t-\tau-|x_1-\xi|/\beta)\right\}\cdot d\tau d\xi dx_1,
\end{aligned}\tag{23}$$

in which L is an arbitrary, convenient, length reference factor, say, the length of the fault, and $\check{G}$ is the nonsingular kernel:

$$\check{G}(x_1,t;\xi,\tau)=\log\left(1+\sqrt{1-\left(\frac{|x_1-\xi|}{\beta(t-\tau)}\right)^2}\right).\tag{24}$$

The form (22) of the last term in Eq.(20) reveals explicitly the various parts that make up the "quasi-static" contribution of the slip to the traction on the fault. Notice that the first term on the right side in Eq.(23) depends on slip-rate only at the wavefront $\tau=t-|x_1-\xi|/\beta$; upon integration over time, the slip-rate $\Delta\dot{u}$ becomes the slip Δu and this term leads to the residual (or static) traction. The second term contains the classical logarithmic singularity in time of the 2D wave equation, and the kernel $\check{G}$ varies only between 0 and $\log 2$. The only singularities that remain are those of the Green's function itself, and these are readily integrable. With the use of Galerkin's method, Cauchy-type integrals no longer appear in the integral representation for the traction.

In light of Eq.(23), it is useful to rewrite Eq.(20) as:

$$\begin{aligned}
&\int_S T(x_1,t)\cdot v(x_1)\cdot dx_1\\
=&-\frac{\rho\beta}{2}\int_S\Delta\dot{u}(x_1,t)\cdot v(x_1)\cdot dx_1\\
&+\frac{\rho\beta}{4}\int_S\int_S\int_0^t\frac{\partial}{\partial\xi}\Delta\ddot{u}(\xi,\tau)\cdot\hat{G}(x_1,t;\xi,\tau)\cdot v(x_1)d\tau d\xi dx_1\\
&-\frac{\mu}{2\pi}\int_S\int_S\int_0^t\left\{\left[\frac{\partial}{\partial\xi}\Delta\dot{u}(\xi,\tau)\cdot\log\frac{|x_1-\xi|}{L}\cdot\frac{\partial}{\partial x_1}v(x_1)-\frac{\partial}{\partial\xi}\Delta\dot{u}(\xi,\tau)\cdot\log\frac{\beta(t-\tau)}{L}\cdot\frac{\partial}{\partial x_1}v(x_1)\right.\right.\\
&-\left.\left.\frac{\partial}{\partial\xi}\Delta\dot{u}(\xi,\tau)\cdot\check{G}(x_1,t;\xi,\tau)\cdot\frac{\partial}{\partial x_1}v(x_1)\right]\cdot H(t-\tau-|x_1-\xi|/\beta)\right\}\cdot d\tau d\xi dx_1,
\end{aligned}\tag{25}$$

in which:

$$\hat{G}(x_1,t;\xi,\tau)=\mathrm{sgn}(x_1-\xi)\left[1-\frac{2}{\pi}\sin^{-1}\left(\frac{|x_1-\xi|}{\beta(t-\tau)}\right)\right]\cdot H\left(t-\tau-|x_1-\xi|/\beta\right).\tag{26}$$

This kernel varies between -1 and 1, with a jump of 2 at $|x_1-\xi|=0$.

To eliminate this jump, we integrate the second integral in Eq.(25) by parts with respect to x_1. This will have the added advantage that discretization in space will then lead to a symmetric matrix. Thus, the term:

$$\begin{aligned}
&\int_S\hat{G}(x_1,t;\xi,\tau)\cdot v(x_1)dx_1\\
=&\int_S\mathrm{sgn}(x_1-\xi)\left[1-\frac{2}{\pi}\sin^{-1}\left(\frac{|x_1-\xi|}{\beta(t-\tau)}\right)\right]H\left(t-\tau-|x_1-\xi|/\beta\right)\cdot v(x_1)dx_1,
\end{aligned}$$

after integration, leads to,

$$\int_S\hat{G}(x_1,t;\xi,\tau)\cdot v(x_1)dx_1=-\int_S\breve{G}(x_1,t;\xi,\tau)\cdot\frac{\partial}{\partial x_1}v(x_1)dx_1,\tag{27}$$

with a continuous bounded kernel $\breve{G}$:

$$\begin{aligned}
&\breve{G}(x_1,t;\xi,\tau)\\
=&\left[(x_1-\xi)\left(1-\frac{2}{\pi}\sin^{-1}\left(\frac{|x_1-\xi|}{\beta(t-\tau)}\right)\right)-\frac{2}{\pi}\sqrt{\beta^2(t-\tau)^2-(x_1-\xi)^2}\right]\cdot H\left(t-\tau-|x_1-\xi|/\beta\right).
\end{aligned}\tag{28}$$

Upon substituting Eq.(27) into Eq.(25), we obtain our final expression for the weak form of the traction.

$$\begin{aligned}
&\int_S T(x_1,t)\cdot v(x_1)\cdot dx_1 \\
=&-\frac{\rho\beta}{2}\int_S \Delta\dot{u}(x_1,t)\cdot v(x_1)\cdot dx_1 \\
&-\frac{\rho\beta}{4}\int_S\int_S\int_0^t \frac{\partial}{\partial\xi}\Delta\ddot{u}(\xi,\tau)\cdot\breve{G}(x_1,t;\xi,\tau)\cdot\frac{\partial}{\partial x_1}v(x_1)d\tau d\xi dx_1 \\
&-\frac{\mu}{2\pi}\int_S\int_S\int_0^t\left\{\left[\frac{\partial}{\partial\xi}\Delta\dot{u}(\xi,\tau)\cdot\log\frac{|x_1-\xi|}{L}\cdot\frac{\partial}{\partial x_1}v(x_1)-\frac{\partial}{\partial\xi}\Delta\dot{u}(\xi,\tau)\cdot\log\frac{\beta(t-\tau)}{L}\cdot\frac{\partial}{\partial x_1}v(x_1)\right.\right. \\
&\left.\left.-\frac{\partial}{\partial\xi}\Delta\dot{u}(\xi,\tau)\cdot\breve{G}(x_1,t;\xi,\tau)\cdot\frac{\partial}{\partial x_1}v(x_1)\right]\cdot H(t-\tau-|x_1-\xi|/\beta)\right\}\cdot d\tau d\xi dx_1,
\end{aligned} \tag{29}$$

From Eq.(29), it is clear that the first two terms yield the dynamic traction and the last term provides a pseudo-static traction. The former terms are proportional to the impedance of the material, $\rho\beta$, whereas the latter is proportional to the shear modulus. The final, or residual, slip is entirely generated by the third term. The only terms that contain singular kernels are (a) the static term, and (b) the one that contains the time-logarithmic singularity, and both can be readily integrated numerically. The kernels $\breve{G}$ and $\breve{G}$ are continuous and bounded.

To solve numerically Eq.(29), we first perform a Galerkin finite element semi-discretization in space, in which we approximate the slip function and the test function in space by the same shape functions $\phi_i(x)$, i.e.,

$$\Delta\dot{u}(x_1,t)=\sum_{i=1}^{N}\phi_i(x)\Delta\dot{u}_i(t), \qquad v(x_1)=\sum_{i=1}^{N}\phi_i(x)v_i, \tag{30}$$

and similarly,

$$T(x_1,t)==\sum_{i=1}^{N}\phi_i(x)T_i(t). \tag{31}$$

Substitution of this approximation into Eq.(29) leads to an equation of the form:

$$\begin{aligned}
\{v\}^T[NN]\{T(t)\}=&\{v\}^T[K_{INS}]\{\Delta\dot{u}(t)\}+\{v\}^T\int_0^t[K_{DYN}(t-\tau)]\{\Delta\ddot{u}(\tau)\}d\tau \\
&+\{v\}^T\int_0^t[K_{QS}(t-\tau)]\{\Delta\dot{u}(\tau)\}d\tau,
\end{aligned} \tag{32}$$

in which $\{v\}$ is an arbitrary vector except for the requirement that it vanish on the boundary of S. $\{\cdot\}$ denotes a column vector, $[\cdot]$ is a matrix, and the superscript T is transpose. $\{T(t)\}$ and $\{\Delta\dot{u}(t)\}$ are time dependent traction and slip-rate vector-valued functions, whose components are the corresponding nodal values. Details of the derivation and expressions for the individual matrices $[NN]$, $[K_{INS}]$, $[K_{DYN}]$, and $[K_{QS}]$ are given in Appendix A. All these matrices are symmetric.

Since Eq.(32) must hold for arbitrary $\{v\}$, it follows that:

$$[NN]\{T(t)\}=[K_{INS}]\{\Delta\dot{u}(t)\}+\int_0^t[K_{DYN}(t-\tau)]\{\Delta\ddot{u}(\tau)\}d\tau+\int_0^t[K_{QS}(t-\tau)]\{\Delta\dot{u}(\tau)\}d\tau. \tag{33}$$

3.2 Numerical verifications

Equation (33) represents the traction distribution in terms of the slip velocity. Thus, Eq.(33) can be used both to evaluate the traction on the fault for the case of a kinematic fault for which the slip function is prescribed, and to solve for the spontaneous rupture along the fault in the case of dynamic rupture. Our primary interest is on the latter. However, we can verify Eq.(33) by prescribing a slip function along the fault and comparing the traction obtained by direct calculation of the convolutions on the right side of the equation against a reference solution.

For our numerical model, we choose a homogeneous full 2D space, with density 2670 kg/m^3 and S-wave velocity 3464 m/s. The prescribed slip-rate function is represented by the following function

$$\Delta\dot{u}(x_1,t)=\phi(x_1)\cdot\psi(t), \tag{34}$$

in which the space function $\phi(x_1)$ and time function $\psi(t)$ are given as,

$$\phi(x_1)=\begin{cases}1-|x_1|/x_d & (|x_1|\le x_d)\\ 0 & (|x_1|>x_d)\end{cases}, \qquad \psi(t)=\begin{cases}0 & (t<0)\\ 16t^2/{t_d}^3 & (0\le t<t_d/4)\\ 2/t_d-16(t-0.5)^2/{t_d}^3 & (t_d/4\le t<3t_d/4)\\ 16(t-t_d)^2/{t_d}^3 & (3t_d/4\le t<t_d)\\ 0 & (t_d\le t)\end{cases}. \tag{35}$$

The parameters x_d and t_d define the shape of the slip-rate function. For the slip-rate $\Delta\dot{u}$, the amplitude of final slip displacement is 1 at $x_1=0$ for all sets of (x_d, t_d). Two prescribed slip cases are selected: Case 1 ($x_d=500$ m, $t_d=0.5$ s) and Case 2 ($x_d=500$ m, $t_d=0.05$ s). The space function is plotted in Fig. 2 and the time function is plotted in Fig. 3.

The residual traction calculated from Eq.(33) is approximated by the solution of the static traction calculated analytically from the final slip displacements $\Delta u_f(x_1) = \phi(x_1)$ because the integration of the time function is defined to be $\int_0^\infty \psi(t)dt = 1$. The reference static traction is,

$$T^S(x_1) = -\frac{\mu}{2\pi}\frac{1}{x_d}\left[\log\left(1+\frac{x_d}{|x_1|}\right)+\log\left|1-\frac{x_d}{|x_1|}\right|\right]. \tag{36}$$

This traction is singular at $x_1 = -x_d$, 0, and x_d, corresponding to the kinks of the prescribed slip distribution. We will compare the calculated residual tractions from Eq.(33) against the reference solution of Eq.(36).

The numerical calculations use a 4000 m long finite fault, divided into uniform elements. The prescribed slip-rate and slip-acceleration are applied at the nodes, and the nodal functions are obtained by solving Eq.(33) as a function of time. The time convolution of Eq.(33) is approximated by a summation at every $0.1t_d$. The nodal tractions are calculated by solving the system of equations Eq.(33) at every 0.01 seconds. The double integrals appearing in the various matrices are approximated by a 5 point Gauss-Legendre integration for the inner integral and 6 points for the outer integral in order to avoid having to evaluate the singular term $\log({x_1}^i - \xi^j)$ when ${x_1}^i = \xi^j$. i and j are the selected point numbers. By reducing integration rules with different number of points for x_1 and ξ, these points never coincide. This will result in some deterioration of the solution. Our primary interest here is to illustrate the applicability of the new boundary integral formulation. Once the validity of the formulation has been established, one can make the process more accurate and efficient; for instance, by using Fourier transforms, not direct time integration, to evaluate the convolutions, and by using ad-hoc integration formulas to evaluate the terms that contain the logarithmic and step functions. This will make it possible to select identical points ${x_1}^i$, ξ^j and t^k, τ^l, with a corresponding increase in accuracy.

Figure 4 shows the approximate residual tractions at $t = 1$ for Case 1. Results are shown for three element sizes: 500 m, 125 m and 31.25 m. The static traction Eq.(36) is also plotted for comparison, but the singularity points are omitted. Clearly, the calculated residual tractions converge to the reference solution with decreasing element size. Because we have used piecewise linear shape functions, approximate solutions provide finite tractions at $x_1 = -x_d$, 0 and x_d, whereas the analytical reference solution goes to infinity.

As a further measure of the approximation quality, we now consider the internal static work. For the reference solution, the exact value is given by:

$$W_i = \frac{1}{2}\int_S \Delta u_f(x_1)\cdot T^S(x_1)\cdot dx_1 = -\frac{\mu}{\pi}\cdot\log(2) = \text{-7,068.8 MJ/m}, \tag{37}$$

where the rigidity $\mu = \rho\beta^2$ is 32,038 MPa. The approximate internal work is given by

$$\tilde{W}_i = \frac{1}{2}\{\Delta u(t)\}^T[NN]\{T(t)\}|_{t=1\,\mathrm{s}}. \tag{38}$$

This yields -7,070.4 MJ/m, -7,067.9 MJ/m and -7,068.3 MJ/m for the examples of the 500 m, 125 m and 31.25 m mesh sizes, respectively. For even the coarsest mesh, the error is less than 0.03 percent. This convergence is consistent with the theoretical behavior of Galerkin's method applied to problems for which the principle of minimum potential energy applies. In such cases, Galerkin's method, for a given mesh, provides the best possible approximation of any numerical method, in the energy norm. This is a clear benefit of applying Galerkin's method to rupture propagation problems, even if the nodal tractions cannot represent the infinite values.

Figure 5 shows the time histories of the tractions at four different locations for both Case 1 and Case 2, for a 31.25 m mesh size. The residual tractions converge to the same distributions in both cases because the prescribed slip displacements have the same final slip distribution. Therefore, the differences between Case 1 and 2 are due to dynamic effects. To examine these in detail, Fig. 5 also shows separate contributions of the instantaneous term, dynamic term and quasi-static term. The instantaneous terms T_{INS} obviously mimic directly the slip-rate functions. The steep slip-rate functions (Case 2) lead to stronger disturbances at the beginning of the traction change for both dynamic and quasi-static terms. After the dynamic disturbances subside, the dynamic terms T_{DYN} converge to zero, and the quasi-static terms T_{QS} converge to finite values. As mentioned previously, the residual tractions depend only on the static terms.

4 SPONTANEOUS RUPTURE PROPAGATION

We now apply the Galerkin boundary integral equation method (GaBIEM) to spontaneous rupture propagation problems, and provide examples of numerical simulations in order to verify the methodology. Numerical results are compared with the traditional BIEM, following the formulation of Cochard and Madariaga (1994).

4.1 Time discretization of the matrix forms

Equation (33) is now a system of integro-differential equation in time. Let $\{\Delta\dot{u}(t)\}$ be the superposition of the prescribed shape function.

$$\{\Delta\dot{u}(t)\} = \sum_{k=1}^{\infty}\{\Delta\dot{u}\}_k\cdot\psi_k(t) = \sum_{k=1}^{\infty}\{\Delta\dot{u}\}_k\cdot\psi_0(t-(k-1)\Delta t), \tag{39}$$

where $\psi_0(t)$ is a prescribed shape function and Δt is a time step. If the prescribed shape function satisfies the causality condition $\psi_0(t \leq 0) = 0$, the summation in Eq.(39) is bounded. Substituting the nodal slip-rate vector into Eq.(33) results in the following system of equations:

$$\begin{aligned}[NN]\{T\}_n =& \sum_{k=1}^{n}[K_{INS}]\psi_0(n\Delta t-(k-1)\Delta t)\cdot\{\Delta\dot{u}\}_k \\ &+\sum_{k=1}^{n}\int_0^{n\Delta t}[K_{DYN}(n\Delta t-\tau)]\dot{\psi}_0(\tau-(k-1)\Delta t)d\tau\cdot\{\Delta\dot{u}\}_k \\ &+\sum_{k=1}^{n}\int_0^{n\Delta t}[K_{QS}(n\Delta t-\tau)]\psi_0(\tau-(k-1)\Delta t)d\tau\cdot\{\Delta\dot{u}\}_k, \\ =&\sum_{k=1}^{n}[K]_{n-k+1}\{\Delta\dot{u}\}_k, \end{aligned} \tag{40}$$

where $\{T\}_n \equiv \{T(n\Delta t)\}$, and

$$[K]_n = [K_{INS}]\psi_0(n\Delta t) + \int_0^{n\Delta t}[K_{DYN}(n\Delta t-\tau)]\dot{\psi}_0(\tau)d\tau + \int_0^{n\Delta t}[K_{QS}(n\Delta t-\tau)]\psi_0(\tau)d\tau. \tag{41}$$

By definition, T is the traction change generated by a given slip distribution. The total traction T_A and initial traction T_I are introduced to represent the traction change $T = T_A - T_I$.

$$[NN]\left[\{T_A\}_n - \{T_I\}\right] = [K]_1\{\Delta\dot{u}\}_n + \sum_{k=1}^{n-1}[K]_{n-k+1}\{\Delta\dot{u}\}_k, \tag{42}$$

where the summation of Eq.(40) is divided into the part of $k < n$ and $k = n$.

4.2 Friction law and contraction of system of equations

Spontaneous rupture propagation problems entail the simulation of the spreading over the rupture area S_r. S_r, a subdomain of the reference whole fault area S, varies with time as slip propagates. The rupture propagation is controlled by a friction law within S_r. Outside, the slip displacement and slip-rate are zero.

A number of friction laws have been proposed over the years. One of the simplest ones is the slip-weakening friction law proposed by Ida (1972). Despite its simplicity, it appears to provide a reasonable representation of the basic behavior of the fault rupture [e.g. Day, 1982]. Day *et al.* (2005) formulated the friction law as follows.

$$T_c - T_A \geq 0, \qquad (T_c - T_A)\Delta\dot{u} = 0 \tag{43}$$

$$T_c = \begin{cases} -\dfrac{T_p - T_r}{D_C}\cdot\Delta u + T_p & (\Delta u < D_C) \\ T_r & (D_C \leq \Delta u) \end{cases}, \tag{44}$$

where T_p is the yield traction, T_r the residual traction and D_C the slip-weakening distance (Fig. 6). The original representation of Eq.(44) is normalized by the compressive normal stress. However, we choose to work with the explicit values because the following numerical calculations do not generate compressive stress changes. Another general representation of slip-weakening friction law is applied as follows.

$$\Delta u(x_1, t) = 0 \qquad (x_1 \in S_s), \tag{45}$$

$$T_A(x_1, t) = f_1(x_1, t)\Delta u(x_1, t) + f_2(x_1, t) \qquad (x_1 \in S_r). \tag{46}$$

Ida's friction law is a special case of the above representation. The matrix form Eq.(46) is constructed as follows.

$$\begin{aligned}\{[NN]\{T_A\}_n\}^R &= \{[F_1]_n\{\Delta u(n\Delta t)\} + \{F_2\}_n\}^R \\ &= \left\{\Psi_0(\Delta t)[F_1]_n\{\Delta\dot{u}\}_n + [F_1]_n\sum_{k=1}^{n-1}\Psi_0((n-k+1)\Delta t)\{\Delta\dot{u}\}_k + \{F_2\}_n\right\}^R, \end{aligned} \tag{47}$$

where $\Psi_0(t)$ is the time integration of $\psi_0(t)$. Details of $[F_1]_n$ and $\{F_2\}_n$ are shown in Appendix B. The notation $\{\cdot\}^R$ is used to denote the contracted vectors consisting of slipping nodes because Eq.(47) is applicable only in S_r.

Equations (42) and (47) provide the following system of equations for $\{\Delta\dot{u}\}_n^R$.

$$\left[\Psi_0(\Delta t)[F_1]_n - [K]_1\right]^R\{\Delta\dot{u}\}_n^R = \{A\}_n^R, \tag{48}$$

where

$$\{A\}_n^R = \left\{\sum_{k=1}^{n-1}[K]_{n-k+1}\{\Delta\dot{u}\}_k + [NN]\{T_I\} - [F_1]_n\sum_{k=1}^{n-1}\Psi_0((n-k+1)\Delta t)\{\Delta\dot{u}\}_k - \{F_2\}_n\right\}^R. \tag{49}$$

The vector $\{A\}_n^R$ consists of the past nodal slip-rate histories, which do not include $\{\Delta\dot{u}\}_n$ at timestep n. Then, the system of equations can be solved for $\{\Delta\dot{u}\}_n$ if $[F_1]_n$ and $\{F_2\}_n$ can be predicted. Only a small number of iterations for a given time step is required because

$[F_1]_n$ and $\{F_2\}_n$ are not determined directly. In this paper, one iteration at every time step is performed because the friction law consists of a piecewise linear function.

To apply the GaBIEM to dynamic rupture, it is also necessary to build in the criterion that controls the transition at the nodal level from non-slip (S_s) to slip (S_r) in order to represent the spreading of the rupture. This algorithm is discussed below, together with the numerical simulations.

4.3 Numerical simulations

Harris *et al.* (2005) have reported a collaborative exercise undertaken to verify numerical simulation methods for spontaneous rupture propagation problems. Their motivation is to compare different computer codes used by scientists at the Southern California Earthquake Center (SCEC). For our application, the benchmark model is modified in order to simulate the simple 2D SH problem, reducing the problem dimensions from three to two.

A planar fault is embedded in a homogeneous full space with density $\rho = 2670$ kg/m^3 and S-wave velocity $\beta = 3464$ m/s. The total length of the fault capable of undergoing antiplane dislocations is 15 km with a 3 km nucleation zone, as shown in Fig.7. The nucleation zone is set to have an initial stress $T_I = 81.6$ MPa, yield stress $T_p = 81.24$ MPa, residual stress $T_r = 63.0$ MPa, and a slip-weakening distance $D_C = 0.4$ m. Outside of the nucleation zone, the initial traction, T_I, is taken to be constant, $T_I = 70.0$ MPa; yield stress $T_p = 81.24$ MPa; residual stress $T_r = 63.0$ MPa; and slip-weakening distance $D_C = 0.4$ m. This model has different static stress drops between the nucleation and non-nucleation regions, while the other parameters are the same.

Table 1 lists the cases considered. The number of elements from one case to another increases by powers of 2, from 128 to 1024. The time steps Δt are controlled by the Courant-Friedrichs-Lewy (CFL) condition, where CFL$= \beta\Delta t/\Delta x$. For now, CFL is set to 0.4. As described already, the double integrals with singular or discontinuous terms included in the various matrices is approximated by 5 points Gauss-Legendre integration for the inner integral and 6 points for the outer integral, and the time convolution is approximated by the summation of the values at the reference time at every $0.1\times$ (time duration of prescribed shape function). The following piecewise linear prescribed shape function $\psi_0(t)$ is chosen to represent the slip-rate function (Eq.(39)) in order to be of the same order as the spatial shape function.

$$\psi_0(t) = \begin{cases} t/\Delta t & (0 < t \le \Delta t) \\ (2\Delta t - t)/\Delta t & (\Delta t < t \le 2\Delta t) \\ 0 & (t \le 0, 2\Delta t < t) \end{cases} \tag{50}$$

The boundary integral equation method (BIEM) developed by Cochard and Madariaga (1994) is used to verify the GaBIEM. GaBIEM and BIEM are denoted by the header names, GA and CM, respectively.

The definition of nucleation zone of the GaBIEM depends on the position of the node. The node located in the nucleation zone is assumed to have higher initial tractions. On the other hand, the zone of the BIEM is controlled by the center of the element because the traction is evaluated only at that point. Then, the nucleation zone is slightly different in all cases, generally by a little less than 3 km. In the following discussion, we focus on the slip-rate functions at $x = 1.5$ km. This location is just next to the nucleation zone.

The selection of rules for nodal slip to represent the rupture is now discussed. Whereas the calculated traction is valid over the entire fault positions, the most accurate values are provided at the Gauss points. For an odd-numbered set, the center of each element will be a Gauss point. This suggests that the traction state, needed to determine whether the traction has exceeded the yield traction, be taken at the center of the elements. In contrast, the slip area must be defined at the node in order to contract the system of equations when arrest of the slip occurs. The initial idea is to select the slipping nodes illustrated in Fig. 8; the element nodes are released when both of the neighboring elements begin to slip. This idea satisfies the causality of rupture front because the slip node is located behind the slipping elements. Figure 9 shows the calculated slip-rate functions at $x = 0.0$ km, 0.5 km, 1.0 km and 1.5 km for GA2 and the reference solution CM4. The evaluated slip-rate functions look similar to CM4, but the rupture starting at $x = 1.5$ km has a steep small peak at about 0.3 seconds. Figure 10 shows a close-up of the slip-rate distribution around the rupture front both before and after the rupture starts. The released node generates a huge slip-rate value. One of the reasons of the steep slip-rate peak is a stress concentration at the pre-released node. The friction law actually helps avoid a stress singularity by introducing the cohesive zone. However, the numerical discretized model does not represent the exact cohesive zone because of the finite-sized element, since the slip-rate distribution has kinks at the rupture front.

We resolve this problem by using another approach. Figure 11 shows an alternative idea for selecting the criterion to release a slipping node. An element node is allowed to slip if at least one of the neighboring elements is slipping. The element located between the slipping and non-slipping elements is assumed to be in a "middle state" between slipping and non-slipping. The friction law essentially models such a middle state region as behaving nonlinearly. This idea introduces one aspect of the friction law into the middle of the elements. Note that this rupture front does not satisfy causality because the slipping nodes are located ahead of the slipping elements. The generated slips are constrained to be only positive in order to prevent the unstable oscillation that might occur because the causality condition is not satisfied. Figure 12 shows the slip-rate histories corresponding to their new criterion illustrated in Fig. 11. The slip-rate function at $x = 1.5$ km now obviously does not have a steep peak at the rupture start. Thus, from now on, we apply the new criterion to represent the rupture fronts in the GaBIEM. Notice that no other filtering, implicit or explicit, is applied to the resulting synthetics.

Figures 13, 14 and 15 show slip-rate, slip displacement and traction time histories at 4 km, located outside the nucleation zone. The rupture propagation spreads from the nucleation zone with an increasing peak slip-rate value. The rupture speed is estimated as 2850 m/s

(about 80 % of S-wave velocity). The simulated slip-rate, slip displacement and traction time histories calculated from both BIEM and GaBIEM converge well with decreasing element size. However, their characteristics of convergence are different. For the larger mesh size, GA1 and GA2 contain small oscillations in the simulated slip-rate functions after the peak. The rupture time, on the other hand, is almost identical to that of CM5. Notice that for CM1 and CM2, even though the resulting slip-rate functions are smooth, their rupture time is faster than for CM5. On the other hand, the rupture time of the GA cases is quite insensitive to the grid size. In addition, the entire slip-rate histories for CM5 and GA4 are practically indistinguishable. As expected, the discrepancies between the two methods for the different element sizes are much less pronounced for the slip displacement, as shown in Fig. 14. In fact, it is noteworthy that the results of GA1, with an element size of 117.2 m, practically coincide with those of CM5, with an element size of 14.65 m. By contrast, the results for CM1 and CM3 for the coarser element sizes exhibit slight early arrivals. A similar behavior is observed for the traction histories (Fig. 15).

4.4 Convergence of the GaBIEM

No exact solutions exist for any dynamic rupture problem, even for the simple two-dimensional one considered here, because of the nonlinearity of the friction law. In order to examine the convergence rate of numerical procedures developed for solving such problems, it becomes necessary to solve the problem repeatedly for increasingly smaller element sizes. Then, one can obtain the rate of convergence empirically by comparing the various solutions. This is the approach that Day *et al.* (2005) used for studying the convergence of a second-order finite difference method and a collocation BIEM method in 3D. They used as a metric the root mean square (RMS) difference between a particular approximation of a given response quantity for various grid sizes and the most accurate approximation obtained with the smallest grid size by the respective method. This approach gives a zero difference for the finest BIEM approximation, even though this approximation, too, contains a numerical error. Here we follow an alternative procedure for selecting the reference solution, which does not suffer from the defect of leading to a zero RMS difference when the decreasing mesh size takes the value of the reference size.

We will study the convergence of the GaBIEM and compare it to that of our implementation of the BIEM of Cochard and Madariaga (1994) [CM]. Since the trial functions for the GaBIEM [GA] differ from those for the CM method, i.e., piecewise constant for CM, and piecewise linear for the GaBIEM both in time and space, we interpolate our numerical solutions, using these trial functions, to evaluate the desired response quantities for a prescribed element size and step-size.

We examine the RMS difference of the slip-rate and slip, as discrete functions of time and space, and of the peak slip-rate over time as a discrete function of space, in the $L2$-norm. To estimate the error, we measure separately the RMS for consecutive, hierarchical approximations of each method, decreasing the element size by one half in each consecutive approximation and then normalize with respect to the best solution obtained with the corresponding method. The meaning of the subscript CM5/GA5 below is that one uses the solution CM5 for the CM method and GA5 for the GaBIEM method. That is,

$$\mathrm{RMS}(\Delta\dot{u}_{[case]}) \equiv \sqrt{\frac{\sum_{i,n}[\Delta\dot{u}^{i,n}_{[case]} - \Delta\dot{u}^{i,n}_{[case+1]}]^2}{N_t \cdot N_x}} \Bigg/ \left(\frac{\sum_{i,n}\Delta\dot{u}^{i,n}_{CM5/GA5}}{N_t \cdot N_x}\right) \tag{51}$$

$$\mathrm{RMS}(\Delta u_{[case]}) \equiv \sqrt{\frac{\sum_{i,n}[\Delta u^{i,n}{}_{[case]} - \Delta u^{i,n}{}_{[case+1]}]^2}{N_t \cdot N_x}} \Bigg/ \left(\frac{\sum_{i,n}\Delta u^{i,n}{}_{CM5/GA5}}{N_t \cdot N_x}\right) \tag{52}$$

$$\mathrm{RMS}(\max(\Delta\dot{u}_{[case]})) \equiv \sqrt{\frac{\sum_{i}[\max_n(\Delta\dot{u}^{i,n}_{[case]}) - \max_n(\Delta\dot{u}^{i,n}_{[case+1]})]^2}{N_x}} \Bigg/ \left(\frac{\sum_{i}\max_n(\Delta\dot{u}^{i,n}_{CM5/GA5})}{N_x}\right), \tag{53}$$

in which, $\sum_{i,n}$ is the double sum over all nodes i and time steps n, and $\sum_i$ is the single sum over all the nodes. $\Delta\dot{u}^{i,n}_{[case]}$ and $\Delta u^{i,n}{}_{[case]}$ are the interpolated slip-rate functions and slip functions at location x_i and instant t_n. The subscript $[case]$ denotes the particular case considered, such as GA1, CM3, etc; $N_t = 2400$ and $N_x = 2048$ are the number of time steps and elements corresponding to CM5. $\max_n(\Delta\dot{u}^{i,n}_{[case]})$ is the peak slip-rate at element i.

This metric allows one to determine independently the rate of convergence of each method in the absence of an exact reference solution. The proof of the validity of this procedure is given in Appendix C. Figure 16 shows the RMS quantities defined by Eqs. (51)-(53) for the GaBIEM and the BIEM methods for four different mesh sizes. The straight line regressions indicate that both methods converge with a power law of the form $c(\Delta x)^\kappa$, where c is a drift component in log scale for a given mesh-size, and κ is the exponent. The values of c and κ for the GA and CM calculations are shown in Table 2. Both Fig.16 and this table show that the convergence rate for the GaBIEM (GA) is faster than that of the BIEM (CM) in all cases, most likely because the GA uses piecewise linear approximations in space and time, whereas CM uses piecewise constant approximations in time and collocation in space. Interestingly, the RMS of the slip-rate distribution and of the slip distribution itself exhibit essentially the same convergence rate, due most likely to the almost singular behavior at the rupture fronts. On the other hand, the RMS of the peak slip-rate converges significantly faster than the other two RMSs. In all cases, the RMS is smaller for the GA for a given mesh size than for the BIEM.

4.5 Execution time comparison of the CM and GA boundary integral equation methods

A basic difference between our formulation of the CM and the GaBIEM methods is that whereas the former is solved in time using an explicit step-by-step integration method, the latter is based on an implicit step-by-step method. Thus, the GaBIEM requires that a system of algebraic equations be solved at each time step, while the CM method requires only matrix-vector product evaluations. On the other hand, whereas for the explicit technique associated with the BIEM, the maximum time step is usually controlled by the CFL stability condition, the implicit technique is unconditionally stable; that is, the maximum time step depends only on the desired accuracy. To examine the numerical and computational performance of the two techniques over time, we now solve again our spontaneous rupture problem for different combinations of the CFL number, $\Delta t = \text{CFL}\cdot\Delta x/\beta$ and element sizes. In a discussion of the stability conditions of the 3D BIEM, Fukuyama and Madariaga (1998) recommended a value CFL = 0.5 for a long asperity model and 0.25 for the circular asperity model. Up to now, we have used CFL = 0.4. In this section we will examine, in addition, the behavior of the GaBIEM for CFL = 1.0, 2.0 and 4.0, for the cases GA2 and GA3, with corresponding element sizes of 58.59 m and 29.30 m, respectively. All our simulations were performed on a single computing node with a 2 GHz Intel Core Duo processor with 2 GB of RAM.

The resulting slip-rate history is shown in Fig. 17 at x=4 km. As mentioned, the GaBIEM remains stable even for CFL = 4.0, though its accuracy deteriorates as CFL increases. Notice especially the severe oscillatory behavior for GA2 and CFL=4.0 and the discrepancy in the rise time with respect to the more accurate solutions. This discrepancy decreases for the case GA3. On the other hand, there are no visible differences between the case GA2 with CFL = 1.0 and the reference case CM5 with CFL = 0.4. i.e., an element size Δx of 58.6 m and Δt = (58.6 m)/β s versus Δx = 14.65 m and Δt = 0.4$\times$(14.65 m)/β s. Based on the results of Day *et al.* (2005), the minimum cohesive length of the cohesive zone for this problem has been estimated as 251 m. That is, with the GaBIEM we resolve the cohesive zone with 4.25 elements.

Figure 18 show results similar to those of Fig. 16, for the case GA and the four values of CFL considered, together with those for the reference case CM. The five cases are denoted as $\text{GA}_{4.0}$, $\text{GA}_{2.0}$, $\text{GA}_{1.0}$, $\text{GA}_{0.4}$, and $\text{CM}_{0.4}$. From these figures, it is clear that the results of $\text{GA}_{1.0}$ are comparable to those of $\text{CM}_{0.4}$. As expected, the accuracy increases for $\text{GA}_{0.4}$ and decreases for $\text{GA}_{4.0}$. Table 3 shows the values of c and κ of the power law for the individual RMSs for all cases.

Finally, to assess the relative computational efficiency for the various cases, the total execution time is listed in Table 4 and plotted in Fig. 19 as a a function of element size. This time increases with mesh size at the same rate for all cases. As expected, it decreases with increasing CFL. For $\text{GA}_{2.0}$, the execution time is slightly less than for $\text{CM}_{0.4}$, which is almost double for $\text{GA}_{1.0}$.

5 CONCLUDING REMARKS

In this formulation of the spontaneous rupture propagation problem for a planar fault embedded in a homogeneous full 2D space, with a slip-weakening friction law, we have presented a Galerkin boundary integral equation method in which the kernel is separated into individual components representing the static, instantaneous, quasi-static, and dynamic contributions. This has the effect of isolating explicitly the weakly singular (logarithmic) terms in space and time, thus leading to a spatial or temporal localization for the corresponding terms. The dynamic and quasi-static contributions are nonlocal, but their kernels are continuous and bounded and their contributions are small compared to those of the other terms. Finite element semidiscretization in space leads to a system of integro-differential equations for the nodal values of the slip rate in time, involving convolutions, in which most of the matrices are diagonally dominant or sparse. These equations have been solved by an implicit, unconditionally stable, step-by-step integration technique.

The numerical and computational performance of the method was examined by means of numerical examples. We have compared the numerical results of the proposed GaBIEM (GA) to those of the traditional BIEM (CM). We found that the rate of convergence of the GA is faster than that of the CM. Also, for the same time-step (CFL = 0.4) and prescribed mesh size, the GA method provides more accurate solutions than the CM method. This improvement in accuracy, however, is at the expense of an increase in the computational time. The execution time required for the $\text{GA}_{0.4}$ is about 6 times longer than that for the $\text{CM}_{0.4}$ case. To obtain GA solutions of comparable accuracy to that of $\text{CM}_{0.4}$, the CFL number for the GA method can be increased to 1.0 ($\text{GA}_{1.0}$). Even though this decreases significantly the execution time, it is still almost double that of the $\text{CM}_{0.4}$ case. It is important to emphasize that in the current implementation of the GaBIEM, we have not yet taken advantage of the separation of the kernels into static, quasi-static, and dynamic components, of the Fast Fourier transform as a solution approach for the convolutions, or of ad-hoc accurate integration formulas for logarithmic singularities, or tried an explicit step-by-step time-integration method, as our main purpose here was to first verify the feasibility of the GaBIEM method. We expect that these improvements will lead to a further increase in accuracy and a reduction in the execution time of the GaBIEM.

ACKNOWLEDGMENTS

We thank the two anonymous reviewers and the editor for their thorough comments. We greatly benefited from their helpful reviews. We thank Prof. Kojiro Irikura, Aichi Institute of Technology, and Prof. Sumio Sawada, Kyoto University, for their encouragement and for providing one of us (HG) with a suitable environment to conduct this work. Part of this work was conducted while HG was a visitor at CMU. This study was supported in part by a Research Fellowship of the Japan Society for the Promotion of Science for Young Scientists (HG) and by

an ITR grant (EAR0326449) (JB) of the U.S. National Science Foundation. Stephen Meacham is the cognizant officer for the NSF project. We are grateful for this support.

REFERENCES

Aagaard, B. T., Hall, J. F. & Heaton T. H., 2001. Characterization of near-source ground motion with earthquake simulations, *Earthquake Spectra*, **17**, 177–207.

Aki, K. & Richards P. G., 2002. *Quantitative Seismology 2nd edn*, University Science Books.

Ampuero, J. P., Vilotte J. P. & Sánchez-Sesma, F. J., 2002. Nucleation of rupture under slip dependent friction law: simple models of fault zone, *J. geophys. Res.,* **107**(B12), 2324, doi:10.1029/2001JB000452.

Andrews, D. J., 1976a. Rupture propagation with finite stress in antiplane strain, *J. geophys. Res.,* **81**, 3575–3582.

Andrews, D. J., 1976b. Rupture velocity of plane-strain shear cracks, *J. geophys. Res.,* **81**, 5679–5687.

Andrews, D. J., 1985. Dynamic plane-strain shear rupture with a slip-weakening friction law calculated by a boundary integral method, *Bull. seism. Soc. Am.,* **75**, 1–21.

Andrews, D. J., 1999. Test of two methods for faulting in finite-difference calculations, *Bull. seism. Soc. Am.,* **89**, 931–937.

Aochi, H. & Fukuyama, E., 2002. Three-dimensional nonplanar simulation of the 1992 Landers earthquake, *J. geophys. Res.,* **107**(B2), 2035, doi:10.1029/2000JB000061.

Ben-Zion, Y. & Rice, J. R., 1997. Dynamic simulations of slip on a smooth fault in an elastic solid, *J. geophys. Res.,* **102**, 17771–17784.

Bouchon, M., 1997. The state of stress on some faults of the San Andreas system as inferred from near-field strong motion data, *J. geophys. Res.,* **102**, 11731–11744.

Brune, J. M., 1970. Tectonic stress and the spectra of seismic shear waves from earthquakes, *J. geophys. Res.,* **75**, 4997–5009.

Chien, D. D. & Atkinson, K. 1997. A discrete Galerkin method for a hypersingular boundary integral equation, *IMA J. Num. Analysis*, **17**, 463–478.

Cochard, A. & Madariaga, R., 1994. Dynamic rupture faulting under rate-dependent friction, *Pure. Appl. Geophys.*, **142**, 419–445.

Das, S., 1980. A numerical method for the estimation of source time functions for general three-dimensional rupture propagation, *Geophys. J. R. astr. Soc.,* **62**, 591–604.

Das, S., 1981. Three-dimensional rupture propagation and implications for the earthquake source mechanism, *Geophys. J. R. astr. Soc.,* **67**, 375–393.

Das, S. & Aki, K., 1977a. A numerical study of two-dimensional spontaneous rupture propagation, *Geophys. J. R. astr. Soc.,* **50**, 643–668.

Das, S. & Aki, K., 1977b. Fault plane with barriers: a versatile earthquake model, *J. geophys. Res.,* **82**, 5658–5670.

Day, S. M., 1982. Three-dimensional simulation of spontaneous rupture: the effect of nonuniform prestress, *Bull. seism. Soc. Am.,* **72**, 1881–1902.

Day, S. M., Dalguer L. A., Lapusta N. & Liu Y., 2005. Comparison of finite difference and boundary integral solutions to three-dimensional spontaneous rupture, *J. geophys. Res.,* **110**, B12307, doi:10.1029/2005JB003813.

Dalguer, L.A, Irikura K. & Riera J., 2003. Generation of new cracks accompanied by the dynamic shear rupture propagation of the 2000 Tottori (Japan) earthquake, *Bull. seism. Soc. Am.,* **93**, 2236–2252.

Dalguer, L. A. & Day S.M., 2006. Comparison of fault representation methods in finite difference simulations of dynamic rupture, *Bull. seism. Soc. Am.,* **96**, 1764–1778.

Dalguer, L. A. & Day, S.M., 2007. Staggered-grid split-node method for spontaneous rupture simulation, *J. geophys. Res.,* **112**, B02302, doi:10.1029/2006JB004467.

Fukuyama, E. & Madariaga, R., 1998. Rupture dynamics of a planar fault in a 3D elastic medium: rate- and slip-weakening friction, *Bull. seism. Soc. Am.,* **88**, 1–17.

Harris, R., Archuleta, R., Aagaard, B., Ampuero, J. P., Andrews, D. J., Bielak, J., Day, S. Dunham, E., Lapusta, N., Oglesby, D., Olsen, K., Pitarka, A. & Rice, J., 2005. A collaborative project: 3D rupture dynamics, validation of the numerical simulation method, *2005 SCEC Progress Report*.

Ida, Y., 1972. Cohesive force across the tip of a longitudinal-shear crack and Griffith's specific surface energy, *J. geophys. Res.,* **77**, 3796–3805.

Kallivokas, L. F., Juneja, T. & Bielak, J., 2005. A symmetric Galerkin BEM variational framework for multi-domain interface problems, *Comput. Methods Appl. Mech. Engrg.*, **194**, 3607–3636.

Koller, M.G., Bonnet, M. & Madariaga, R., 1992. Modeling of dynamical crack propagation using time-domain boundary integral equations, *Wave Motion*, **16**, 339–366.

Kostrov, B.V. & Das S., 1989. *Principles of earthquake source mechanics*, Cambridge University Press.

Lapusta, N., Rice, J. R., Ben-Zion, Y. & Zheng, G., 2000. Elastodynamic analysis for slow tectonic loading with spontaneous rupture episodes on faults with rate- and state-dependent friction, *J. geophys. Res.,* **105**, 23765–23789.

Lapusta, N. & Rice, J. R., 2003. Nucleation and early seismic propagation of small and large events in a crustal earthquake model, *J. geophys. Res.,* **108**(B4), 2205, doi:10.1029/2001JB000793.

Li, S., Mear, M. E. & Xiao, L., 1998. Symmetric weak-form integral equation method for three-dimensional fracture analysis, *Comput. Methods Appl. Mech. Engrg.*, **151**, 435–459.

Madariaga, R., 1976. Dynamics of an expanding circular fault, *Bull. seism. Soc. Am.,* **66**, 639–667.

Madariaga, R., 1977. High-frequency radiation from crack (stress drop) models of earthquake faulting, *Geophys. J. R. astr. Soc.,* **51**, 625–651.

Madariaga, R., 1979. On the relation between seismic moment and stress drop in the presence of stress and strength heterogeneity, *J. geophys. Res.,* **84**, 2243–2250.

Madariaga, R., Olsen, K. B. & Archuleta, R. J., 1998. Modeling dynamic rupture in a 3D earthquake fault model, *Bull. seism. Soc. Am.,* **88**, 1182–1197.

Oglesby, D. D. & Archuleta, R. J., 2000a. Dynamics of dip-slip faulting: explorations in two dimensions, *J. geophys. Res.,* **105**, 13643–13653.

Oglesby, D. D., Archuleta, R. J. and Nielsen, S. B., 2000b. The three-dimensional dynamics of dipping faults, *Bull. seism. Soc. Am.,* **90**, 616–628.

Oglesby, D. D. & Archuleta, R. J., 2003. The three-dimensional dynamics of a nonplanar thrust fault, *Bull. seism. Soc. Am.,* **93**, 2222–2235.

Ohnaka, M. & Kuwahara, Y., 1990. Characteristic features of local breakdown near a crack-tip in the transition zone from nucleation to unstable rupture during stick-slip shear failure, *Tectonophysics,* **175**, 197–220.

Tada, T. & Yamashita, T., 1997. Non-hypersingular boundary integral equations for two-dimensional non-planar crack analysis, *Geophys. J. Int.,* **130**, 269–282.

Tada, T., Fukuyama, E. & Madariaga, R., 2000. Non-hypersingular boundary integral equations for 3-D non-planar crack dynamics, *Computational Mechanics*, **25**, 613–626.

Yoshida, K., Nishimura, N. & Kobayashi, S., 2001. Application of fast multipole Galerkin boundary integral equation method to elastostatic crack problems in 3D, *Int. J. Numer. Meth. Engrg.*, **50**, 525–547.

Zeng, X. & Bielak, J., 1994. Exterior stable domain segmentation integral equation method for scattering problems, *Int. J. Numer. Meth. Engrg.*, **37**, 777–792.

Zhang, H. & Chen, X., 2006. Dynamic rupture on a planar fault in three-dimensional half space -I. Theory, *Geophys. J. Int.,* **164**, 633–652.
Zhang, H. & Chen, X., 2006. Dynamic rupture on a planar fault in three-dimensional half space -II. Validations and numerical experiments, *Geophys. J. Int.,* **164**, 917–932.

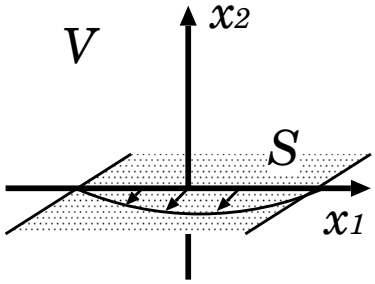

Figure 1. Planar fault S embedded in homogeneous full 2D space V.

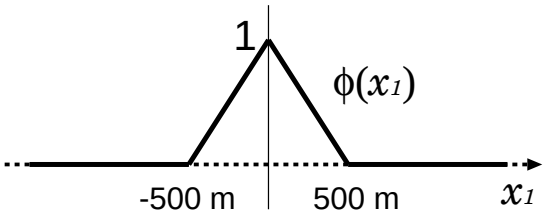

Figure 2. Space distribution of the prescribed final slip displacement.

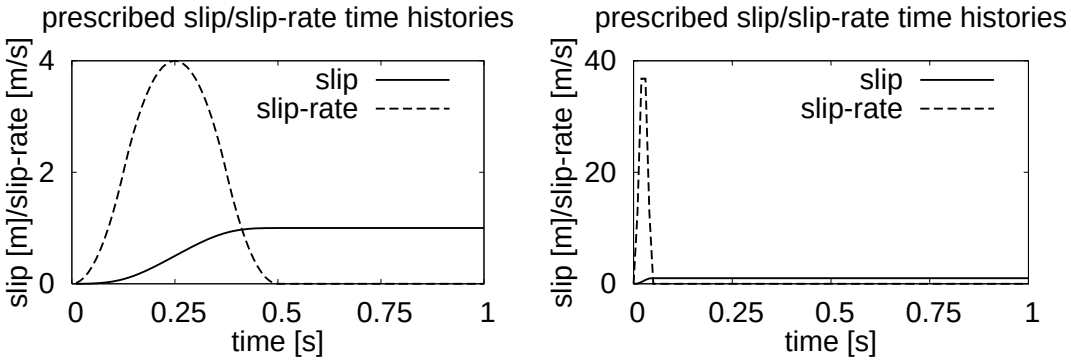

(a) Case 1 (b) Case 2

Figure 3. Time histories of the prescribed slip displacement and slip-rate $\psi(t)$.

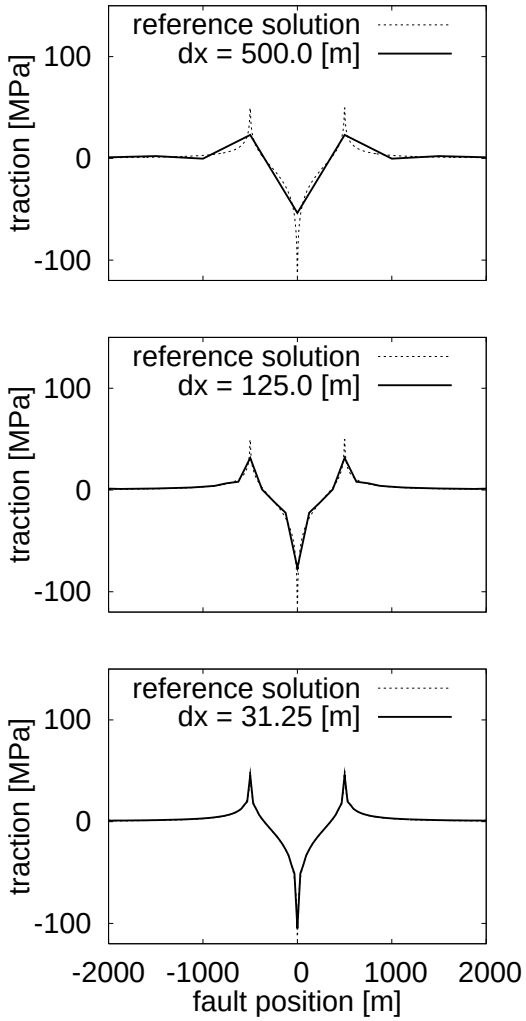

Figure 4. Calculated and exact residual traction distributions for different grid sizes for numerical verification of Eq.(33) for a kinematic source. The calculated residual traction distribution converges to the reference solution with decreasing the element size.

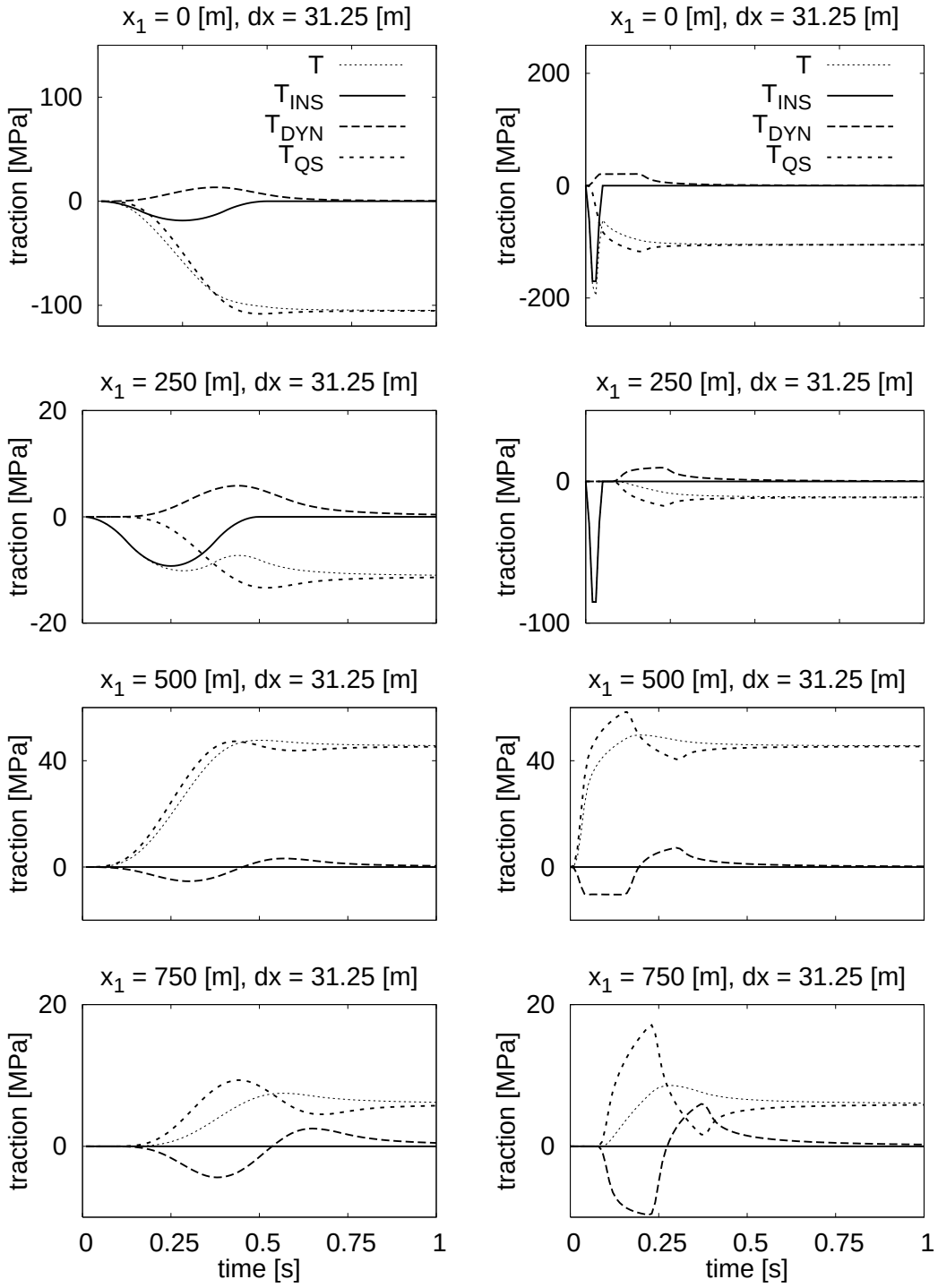

(a) Case 1 (b) Case 2

Figure 5. Contributions of each traction term represented by the traction time histories at $x_1 = 0$ m, 250 m, 500 m and 750 m. T is the total traction, T_{INS} the instantaneous term, T_{DYN} the dynamic term and T_{QS} the quasi-static term. Case 1 ($x_d = 500$ m, $t_d = 0.5$ s), Case 2 ($x_d = 500$ m, $t_d = 0.05$ s)

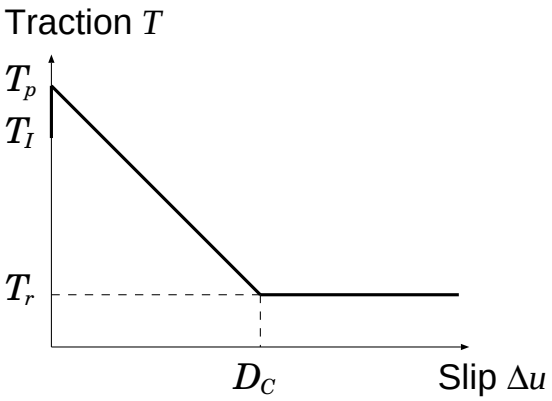

Figure 6. Simple slip-weakening friction law [Ida 1972]. T_p, T_I, T_r, and D_C are a yield traction, an initial traction, a residual traction and a slip-weakening distance.

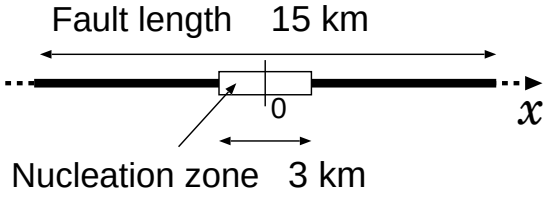

Figure 7. Fault dimension and the location of nucleation zone for numerical simulation.

Table 1. Numerical models used to simulate the spontaneous rupture propagation. The BIEM developed by Cochard and Madariaga's (1994) method is adopted as the reference method. GA denotes the GaBIEM. CM refers to our implementation of the Cochard and Madariaga formulation.

Case	element size Δx [m]	number of elements	time step Δt [s]	CFL$=\beta\Delta t/\Delta x$	Method
GA1	117.20	128	0.0135	0.4	GaBIEM
GA2	58.59	256	0.0068	0.4	GaBIEM
GA3	29.30	512	0.0034	0.4	GaBIEM
GA4	14.65	1024	0.0017	0.4	GaBIEM
GA5	7.324	2048	0.0008	0.4	GaBIEM
CM1	117.20	128	0.0135	0.4	BIEM
CM2	58.59	256	0.0068	0.4	BIEM
CM3	29.30	512	0.0034	0.4	BIEM
CM4	14.65	1024	0.0017	0.4	BIEM
CM5	7.324	2048	0.0008	0.4	BIEM

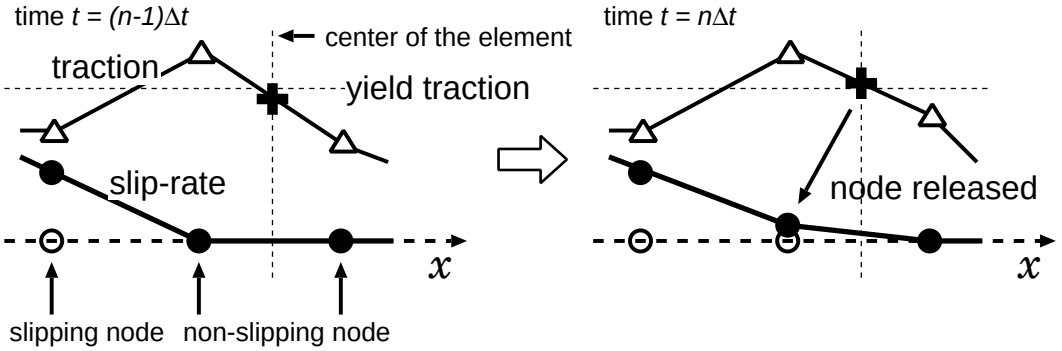

Figure 8. Illustration of one procedure to shift the rupture front. The rupture start is assessed at the center of each element. The reference node is released if both neighboring elements are slipping.

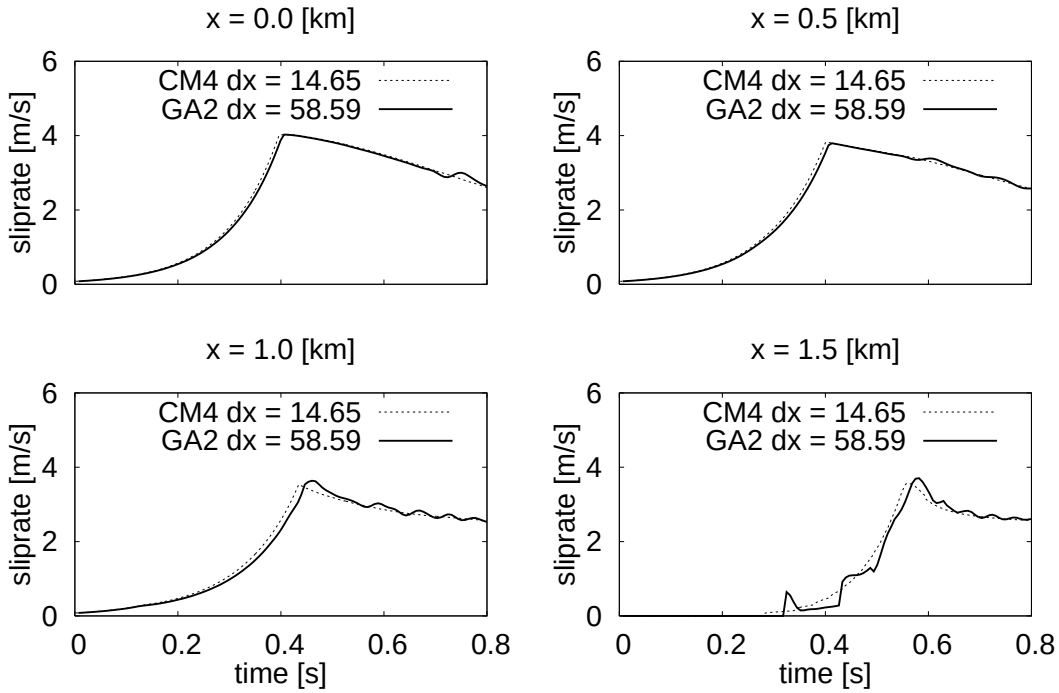

Figure 9. Slip-rate time histories of GA2 and CM4 to compare the behavior around the rupture start by using the idea of Fig. 8. The slip-rate functions are compared at $x = 0$ km, 0.5 km, 1.0 km and 1.5 km

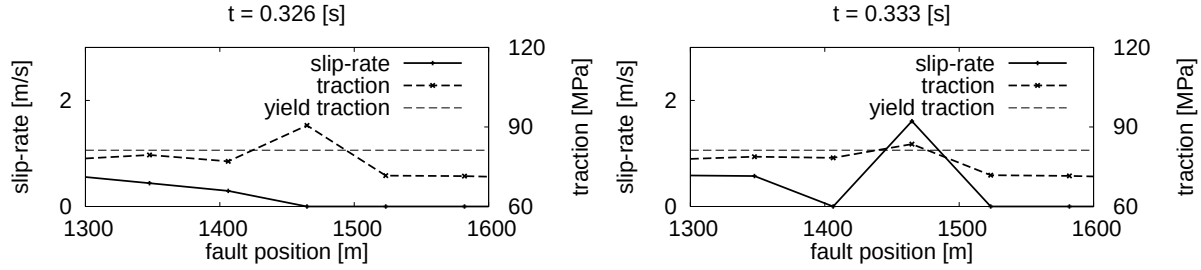

Figure 10. Snapshots of slip-rate and traction distribution at $t = 0.326$ s and 0.333 s based on the idea of Fig. 8. The rupture front is spreading to the right, while the large slip-rate value is observed at the rupture front.

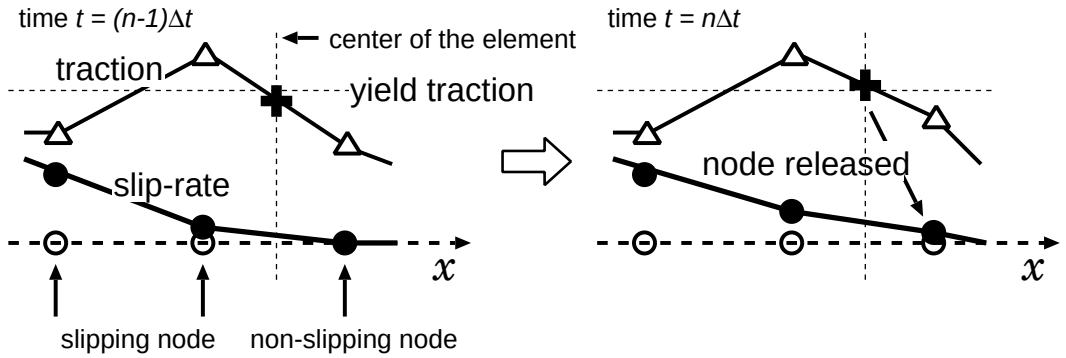

Figure 11. Illustration of the second procedure used to shift the rupture front. The rupture start is assessed at the center of the elements. If at least one of the neighboring elements is slipping, the reference node is released. This is the procedure adopted in the sequel.

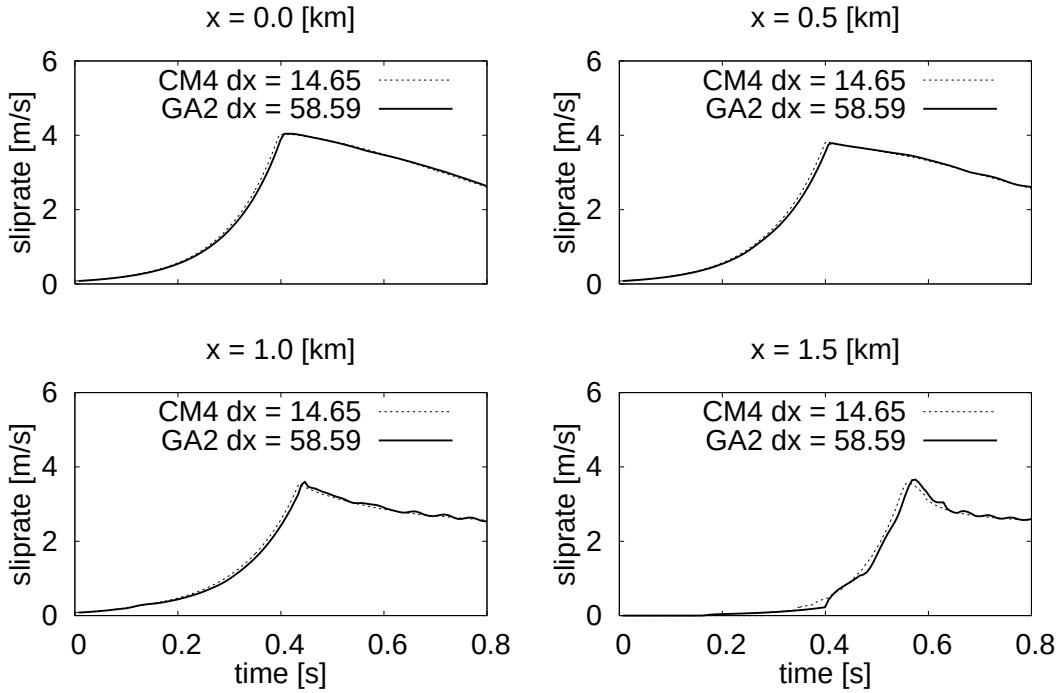

Figure 12. Slip-rate time histories of GA2 and CM4 to compare the behavior near the inception of rupture. The rupture criterion of the GaBIEM is that shown in Fig. 11. The slip-rate functions are compared at $x = 0$ km, 0.5 km, 1.0 km and 1.5 km.

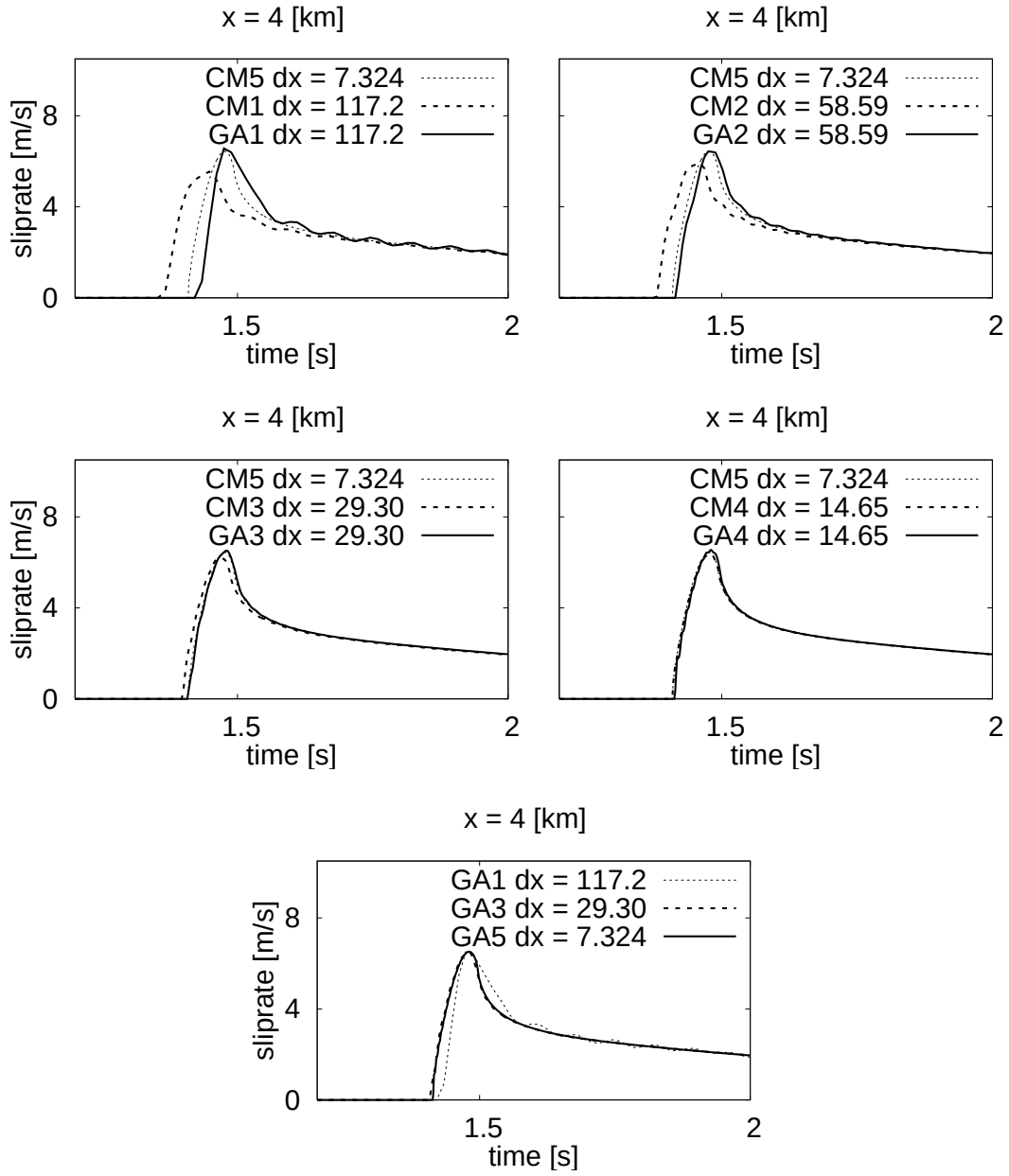

Figure 13. Slip-rate time histories at $x = 4$ km on the fault. Top two rows correspond to GA1/CM1, GA2/CM2, GA3/CM3 and GA4/CM4 cases. The slip-rate histories of CM5 are also plotted as the reference solution. The bottom row shows the comparison between the GA1, GA3 and GA5 cases.

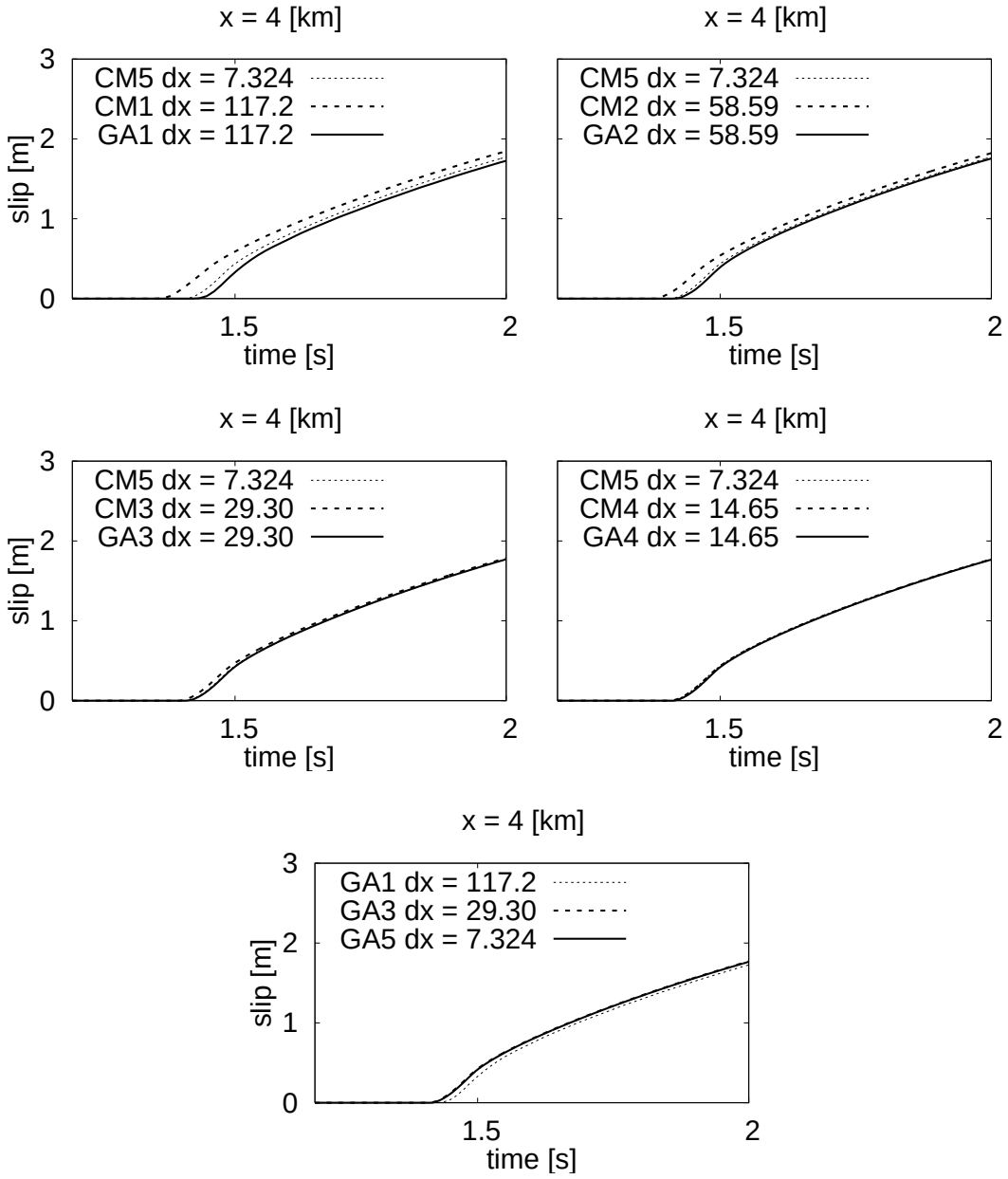

Figure 14. Slip displacement time histories at $x = 4$ km on the fault. Top two rows correspond to GA1/CM1, GA2/CM2, GA3/CM3 and GA4/CM4 cases. The slip displacement of CM5 are also plotted as the reference solution.The bottom row shows the comparison between the GA1, GA3 and GA5 cases.

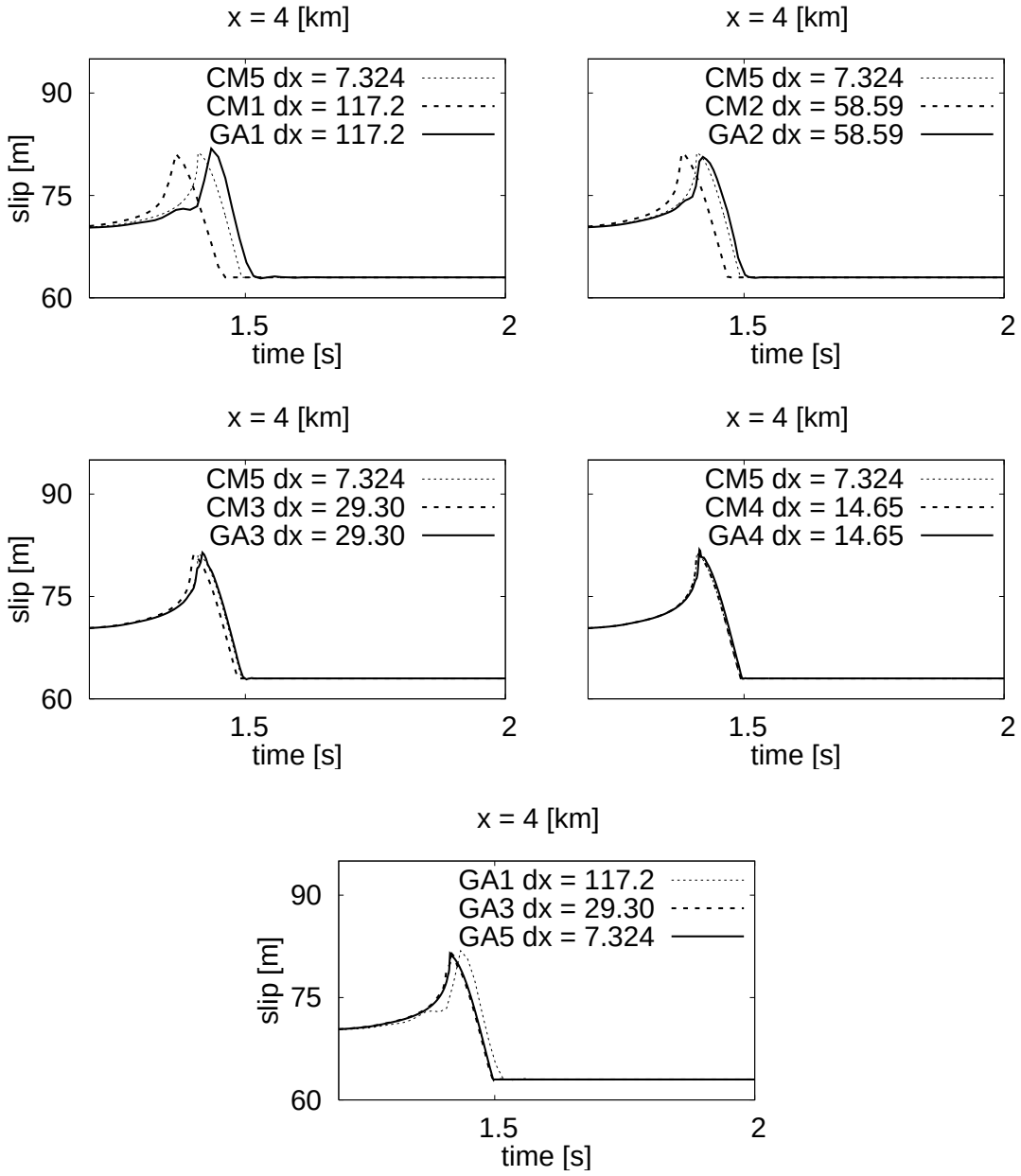

Figure 15. Traction time histories at $x = 4$ km on the fault. Top two rows correspond to GA1/CM1, GA2/CM2, GA3/CM3 and GA4/CM4 cases. The traction histories of CM5 are also plotted as the reference solution. The bottom row shows the comparison between the GA1, GA3 and GA5 cases.

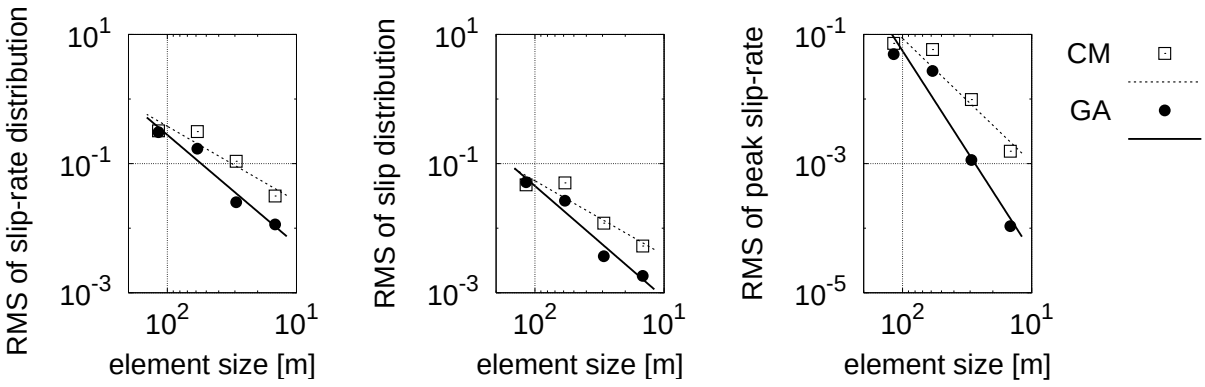

Figure 16. Verification of the RMS of the slip-rate (left) and slip distribution (middle) and the RMS of the peak slip-rate (right) with element size, for the GaBIEM (GA) and BIEM (CM) methods [Eqs. (51)-(53)]. Each panel also shows the straight lines obtained from the regressions from the discrete calculated values.

Table 2. Convergence rates of GaBIEM(GA) and BIEM(CM) method

Method	RMS slip-rate		RMS slip		RMS peak slip-rate	
	c	κ	c	κ	c	κ
CM	1.8×10^{-1}	1.16	2.7×10^{-2}	1.15	7.3×10^{-6}	2.12
GA	1.1×10^{-2}	1.70	1.6×10^{-3}	1.73	2.8×10^{-8}	3.27

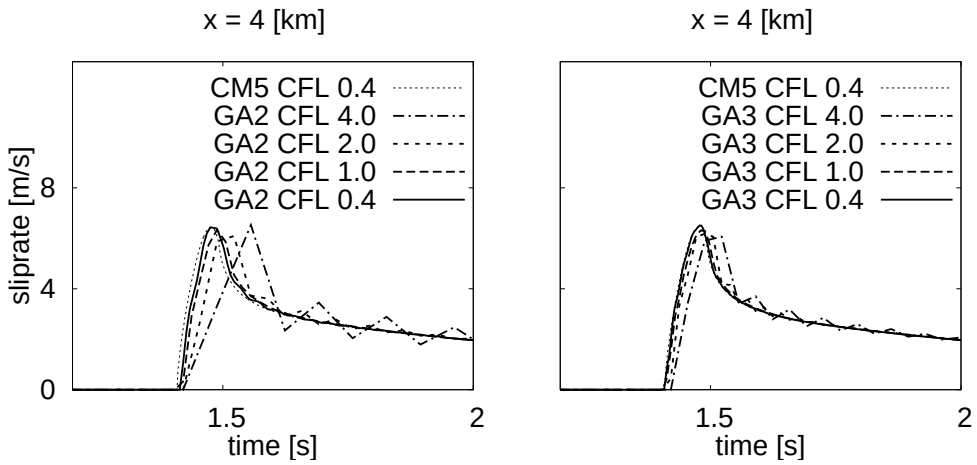

Figure 17. Verification of the RMS of the slip-rate (left) and slip distribution (middle) and the RMS of the peak slip-rate (right) with element size like Fig. 16, for the GaBIEM (GA) (for different values of the CFL factor) and BIEM (CM) (for CFL=0.4) [Eqs. (51)-(53)]. Each panel also shows the straight lines obtained from the regressions from the discrete calculated values.

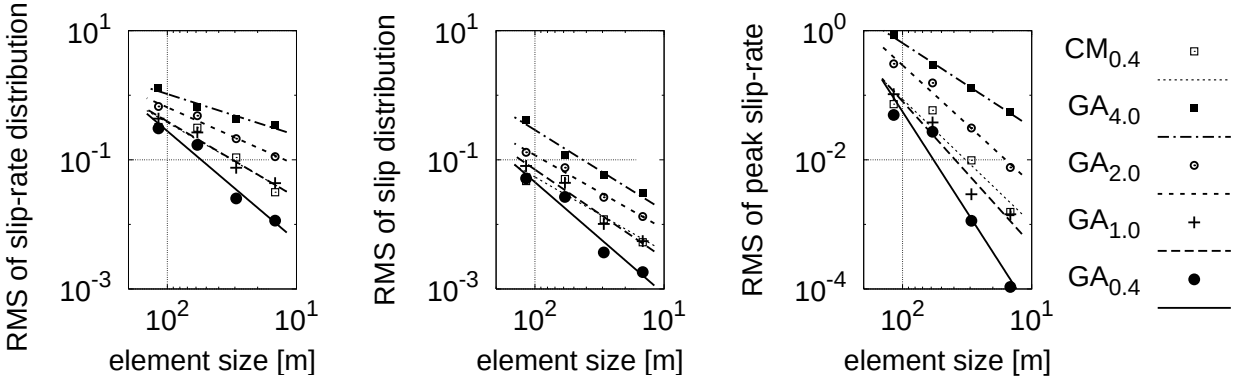

Figure 18. RMS with element size for different to CFL numbers [Eqs.(51)-(53)]. (left) slip-rate time and space distributions, (middle) slip displacement time and space distributions, and (right) peak slip-rate space distributions.

Table 3. Convergence rates of different CFL cases denoted as $\mathrm{GA}_{4.0}$, $\mathrm{GA}_{2.0}$, $\mathrm{GA}_{1.0}$, $\mathrm{GA}_{0.4}$, and $\mathrm{CM}_{0.4}$

Method	RMS slip-rate		RMS slip		RMS peak slip-rate	
	c	κ	c	κ	c	κ
$\mathrm{CM}_{0.4}$	1.8×10^{-1}	1.16	2.7×10^{-2}	1.15	7.3×10^{-6}	2.12
$\mathrm{GA}_{4.0}$	0.55×10^{-1}	0.64	9.2×10^{-2}	1.25	1.1×10^{-4}	2.25
$\mathrm{GA}_{2.0}$	0.11×10^{-1}	0.89	6.1×10^{-2}	1.14	1.7×10^{-5}	2.33
$\mathrm{GA}_{1.0}$	1.7×10^{-1}	1.18	1.3×10^{-2}	1.37	6.6×10^{-7}	2.78
$\mathrm{GA}_{0.4}$	1.1×10^{-2}	1.70	1.6×10^{-3}	1.73	2.8×10^{-8}	3.27

Table 4. Calculation times of each simulation, BIEM CFL=0.4 ($CM_{0.4}$), GaBIEM CFL=0.4 ($GA_{0.4}$), GaBIEM CFL=1.0 ($GA_{1.0}$), GaBIEM CFL=2.0 ($GA_{2.0}$) and GaBIEM CFL=4.0 ($GA_{4.0}$) cases.

Case	Δx = 117.20 m	Δx = 58.59 m	Δx = 29.30 m	Δx = 14.65 m	Δx = 7.324 m
$GA_{4.0}$	0.9 s	4.0 s	3.4×10^{1} s	2.7×10^{2} s	3.0×10^{3} s
$GA_{2.0}$	1.8 s	9.0 s	6.1×10^{1} s	4.9×10^{2} s	5.8×10^{3} s
$GA_{1.0}$	4.0 s	2.3×10^{1} s	1.7×10^{2} s	1.4×10^{3} s	1.3×10^{4} s
$GA_{0.4}$	1.1×10^{1} s	7.9×10^{1} s	6.2×10^{2} s	5.3×10^{3} s	3.5×10^{4} s
$CM_{0.4}$	2.3 s	1.2×10^{1} s	8.3×10^{1} s	6.9×10^{2} s	5.9×10^{3} s

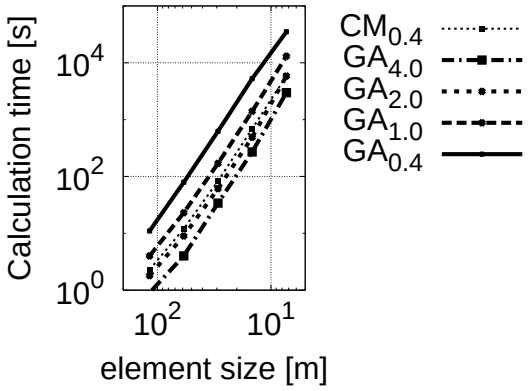

Figure 19. Comparison of calculation times of each simulation, BIEM CFL=0.4 ($CM_{0.4}$), GaBIEM CFL=0.4 ($GA_{0.4}$), GaBIEM CFL=1.0 ($GA_{1.0}$), GaBIEM CFL=2.0 ($GA_{2.0}$) and GaBIEM CFL=4.0 ($GA_{4.0}$) cases.

APPENDIX A: DISCRETIZATION OF GALERKIN METHOD IN MATRIX FORM

Let element S_e ($e = 1, \cdots, N_x$) be a sub-domain $[{x^1}_e, {x^2}_e]$ of S ($S = S_1 \cup \cdots \cup S_{N_x}$). Slip displacement, traction and test function in the element S_e are approximated in space by the same linear shape functions ${N^1}_e(x_1)$ and ${N^2}_e(x_1)$ as follows.

$$\begin{aligned} \Delta u(x_1,t) &= \Delta {u^1}_e(t){N^1}_e(x_1) + \Delta {u^2}_e(t){N^2}_e(x_1) \\ T(x_1,t) &= {T^1}_e(t){N^1}_e(x_1) + {T^2}_e(t){N^2}_e(x_1) \\ v(x_1) &= {v^1}_e{N^1}_e(x_1) + {v^2}_e{N^2}_e(x_1), \end{aligned} \tag{A1}$$

where $\Delta {u^1}_e$, $\Delta {u^2}_e$, ${T^1}_e$, ${T^2}_e$, ${v^1}_e$ and ${v^2}_e$ are the nodal values of Δu, T and v at $x_1 = {x^1}_e$ and ${x^2}_e$, respectively.

$${N^1}_e(x_1) = \begin{cases} ({x^2}_e - x_1)/\Delta x_e & (x_1 \in S_e) \\ 0 & (x_1 \notin S_e) \end{cases}, \qquad {N^2}_e(x_1) = \begin{cases} (x_1 - {x^1}_e)/\Delta x_e & (x_1 \in S_e) \\ 0 & (x_1 \notin S_e) \end{cases}, \tag{A2}$$

where $\Delta x_e = {x^2}_e - {x^1}_e$.

These approximations provide the discretized forms of the integral equation Eq.(29). Left hand side of Eq.(29) is represented as follows.

$$\begin{aligned} &\int_S T(x_1,t)\cdot v(x_1)\cdot dx_1 \\ =&\sum_e \int_{S_e} \left[{T^1}_e(t){N^1}_e(x_1) + {T^2}_e(t){N^2}_e(x_1)\right]\cdot\left[{v^1}_e{N^1}_e(x_1) + {v^2}_e{N^2}_e(x_1)\right] dx_1 \\ =&\sum_e \int_{S_e} \left\{{T^1}_e(t), {T^2}_e(t)\right\} \begin{bmatrix} {N^1}_e(x_1){N^1}_e(x_1), & {N^1}_e(x_1){N^2}_e(x_1) \\ {N^2}_e(x_1){N^1}_e(x_1), & {N^2}_e(x_1){N^2}_e(x_1) \end{bmatrix} \begin{Bmatrix} {v^1}_e \\ {v^2}_e \end{Bmatrix} dx_1 \\ =&\sum_e \{T_e(t)\}^T [NN_e]\{v_e\}, \end{aligned} \tag{A3}$$

where $\{T_e(t)\}^T = \{{T^1}_e(t), {T^2}_e(t)\}$, $\{v_e\}^T = \{{v^1}_e, {v^2}_e\}$ and

$$[NN_e] = \begin{bmatrix} \int_{S_e} {N^1}_e(x_1){N^1}_e(x_1)dx_1, & \int_{S_e} {N^1}_e(x_1){N^2}_e(x_1)dx_1 \\ \int_{S_e} {N^2}_e(x_1){N^1}_e(x_1)dx_1, & \int_{S_e} {N^2}_e(x_1){N^2}_e(x_1)dx_1 \end{bmatrix} \equiv \left[\int_{S_e} {N^\alpha}_e(x_1){N^\beta}_e(x_1)dx_1\right]. \tag{A4}$$

We use the final expression of Eq.(A4) to represent the corresponding matrices. The integrations of the right hand side of Eq.(29) is discretized as follows.

$$-\frac{\rho\beta}{2}\int_S \Delta\dot{u}(x_1,t)\cdot v(x_1)\cdot dx_1 = \sum_e \{\Delta\dot{u}_e(t)\}^T[K_{INSe}]\{v_e\} \tag{A5}$$

$$-\frac{\rho\beta}{4}\int_S\int_S\int_0^t \frac{\partial}{\partial\xi}\Delta\ddot{u}(\xi,\tau)\breve{G}(x_1,t;\xi,\tau)\frac{\partial}{\partial x_1}v(x_1)d\tau d\xi dx_1 = \int_0^t \sum_{e,f}\{\Delta\ddot{u}_e(\tau)\}^T[K_{DYN}(t-\tau)_{e,f}]\{v_f\}d\tau \tag{A6}$$

$$-\mu^2\int_S\int_S\int_0^t \frac{\partial}{\partial\xi}\Delta\dot{u}(\xi,\tau)\bar{G}(x_1,t;\xi,\tau)\frac{\partial}{\partial x_1}v(x_1)d\tau d\xi dx_1 = \int_0^t \sum_{e,f}\{\Delta\dot{u}_e(\tau)\}^T[K_{QS}(t-\tau)_{e,f}]\{v_f\}d\tau, \tag{A7}$$

where

$$[K_{INSe}] = \left[-\frac{\rho\beta}{2}\int_{S_e} {N^\alpha}_e(x_1){N^\beta}_e(x_1)dx_1\right] \tag{A8}$$

$$[K_{DYN}(t)_{e,f}] = \left[-\frac{\rho\beta}{4}\int_{S_e}\int_{S_f}\frac{\partial}{\partial\xi}{N^\alpha}_e(\xi)\breve{G}(x_1,t;\xi,0)\frac{\partial}{\partial x_1}{N^\beta}_f(x_1)dx_1 d\xi\right] \tag{A9}$$

$$[K_{QS}(t)_{e,f}] = \left[-\mu^2\int_{S_e}\int_{S_f}\frac{\partial}{\partial\xi}{N^\alpha}_e(\xi)\bar{G}(x_1,t;\xi,0)\frac{\partial}{\partial x_1}{N^\beta}_f(x_1)dx_1 d\xi\right]. \tag{A10}$$

The integrations in the matrices Eqs.(A4), (A8), (A9) and (A10) are calculated numerically by Gauss-Legendre method. However, the integrand of (A10) has infinite values at $x_1 = \xi$. Therefore, we use the following analytical integrated result for the case of $e = f$.

$$\begin{aligned} [K_{QS}(t)_{e,e}] = \Big[&(-1)^{\alpha+\beta}\frac{\mu}{2\pi}\Big[\left\{\pi\nu - \nu\sqrt{\nu^2-1} + \log(\nu - \sqrt{\nu^2-1}) - 2\nu\sin^{-1}(1/\nu)\right\}H(\nu-1) \\ &- \left\{\pi\nu - \nu^2\right\}\Big]\Big], \end{aligned} \tag{A11}$$

where $\nu = \beta t/\Delta x_e$.

Each component of the element matrices is relocated to components of global matrices. Then, the integral equation Eq.(29) is discretized as the matrix form Eq.(32).

APPENDIX B: MATRIX FORM OF FRICTION LAW

Eq.(46) is equivalent to the following weak form.

$$\int_S T_A(x_1,t)\cdot v(x_1)\cdot dx_1 = \int_S f_1(x_1,t)\Delta u(x_1,t)\cdot v(x_1)\cdot dx_1 + \int_S f_2(x_1,t)\cdot v(x_1)\cdot dx_1. \tag{B1}$$

The left hand side of the equation is approximated by the same representation of Eq.(A3).

$$\int_S T_A(x_1,t)\cdot v(x_1)\cdot dx_1 = \sum_e \{T_{A_e}(t)\}^T [NN_e]\{v_e\}. \tag{B2}$$

The frictional parameters are assumed to be constant in the elements.

$$\int_S f_1(x_1,t)\Delta u(x_1,t)\cdot v(x_1)\cdot dx_1 = \sum_e f_{1_e}(t)\{\Delta u_e(t)\}^T [NN_e]\{v_e\} \tag{B3}$$

$$\int_S f_2(x_1,t)\cdot v(x_1)\cdot dx_1 = \sum_e f_{2_e}(t)\{N_e\}^T\{v_e\}. \tag{B4}$$

where scalar $f_{1_e}(t)$ and $f_{2_e}(t)$ are the frictional parameters of element e. $\{N_e\}$ is a vector.

$$\{N_e\}^T = \left\{\int_{S_e} {N^1}_e(x_1)dx_1, \int_{S_e} {N^2}_e(x_1)dx_1\right\}^T. \tag{B5}$$

Here, we define $[F_{1_e}]_n$ and $\{F_{2_e}\}_n$ as

$$[F_{1_e}]_n \equiv f_{1_e}(n\Delta t)[NN_e] \tag{B6}$$

$$\{F_{2_e}\}_n \equiv f_{2_e}(n\Delta t)\{N_e\}. \tag{B7}$$

Each component of the element matrices and vectors is relocated to the components of the global matrices, named $[F_1]_n$ and $\{F_2\}_n$. This leads to Eq.(47).

APPENDIX C: ERROR ESTIMATE FOR RMS DEFINED BY EQS. (51)-(53)

We provide here the proof of the order of convergence for both the BIEM and the GaBIEM numerical simulation methods. The definitions of RMS contain no exact or approximations to the exact solutions as reference values.

The RMS defined by Eqs. (51)-(53) for a hierarchical sequence of mesh refinements can be written as follows:

$$\text{RMS}(\Delta x) \equiv ||\boldsymbol{u}(\Delta x) - \boldsymbol{u}(\alpha\Delta x)||_{L_2}, \tag{C1}$$

where $\boldsymbol{u}$ is the vector consisting of the numerical solutions at the reference points distributed in space and time. Δx is the element size, and α is a constant, which is set to be $1/2$ in this work.

Let the numerical solutions converge as $(\Delta x)^\kappa$. Then:

$$||\boldsymbol{u}(\Delta x) - \bar{\boldsymbol{u}}||_{L_2} \le c_1(\Delta x)^\kappa, \tag{C2}$$

$$||\boldsymbol{u}(\alpha\Delta x) - \bar{\boldsymbol{u}}||_{L_2} \le c_1(\alpha\Delta x)^\kappa, \tag{C3}$$

where $\bar{\boldsymbol{u}}$ is the vector of the exact solutions, and c_1 is a constant, independent of Δx. From the representation of RMS as Eq.(C1), the estimated numerical error of RMS can be written in the following form:

$$||\boldsymbol{u}(\Delta x) - \boldsymbol{u}(\alpha\Delta x)||_{L_2} = ||(\boldsymbol{u}(\Delta x) - \bar{\boldsymbol{u}}) - (\boldsymbol{u}(\alpha\Delta x) - \bar{\boldsymbol{u}})||_{L_2}. \tag{C4}$$

By the triangle inequality, it follows that:

$$\begin{aligned}\text{RMS}(\Delta x) &\le ||\boldsymbol{u}(\Delta x) - \bar{\boldsymbol{u}}||_{L_2} + ||\boldsymbol{u}(\alpha\Delta x) - \bar{\boldsymbol{u}}||_{L_2},\\ \text{RMS}(\Delta x) &\le c_1(1+\alpha^\kappa)(\Delta x)^\kappa \equiv c(\Delta x)^\kappa.\end{aligned} \tag{C5}$$

Therefore, the RMS also represents the order of convergence of the numerical solutions. Since in Fig. 16 and 18 we plot $\log(\text{RMS})$ vs. $\log(\Delta x)^{-1}$, the negative slope provides the order of convergence κ.